

Planck Early Results 21: Properties of the interstellar medium in the Galactic Plane

Planck Collaboration: A. Abergel⁴⁷, P. A. R. Ade⁷², N. Aghanim⁴⁷, M. Arnaud⁵⁸, M. Ashdown^{56,4}, J. Aumont⁴⁷, C. Baccigalupi⁷⁰, A. Balbi²⁸, A. J. Banday^{76,7,63}, R. B. Barreiro⁵³, J. G. Bartlett^{3,54}, E. Battaner⁷⁸, K. Benabed⁴⁸, A. Benoit⁴⁶, J.-P. Bernard^{76,7}, M. Bersanelli^{52,41}, R. Bhatia⁵, J. J. Bock^{54,8}, A. Bonaldi³⁷, J. R. Bond⁶, J. Borrill^{62,73}, F. R. Bouchet⁴⁸, F. Boulanger⁴⁷, M. Bucher³, C. Burigana⁴⁰, P. Cabella²⁸, J.-F. Cardoso^{59,3,48}, A. Catalano^{3,57}, L. Cayón¹⁸, A. Challinor^{50,56,10}, A. Chamballu⁴⁴, L.-Y. Chiang⁴⁹, C. Chiang¹⁷, P. R. Christensen^{67,29}, S. Colombi⁴⁸, F. Couchot⁶¹, A. Coulais⁵⁷, B. P. Crill^{54,68}, F. Cuttaia⁴⁰, T. M. Dame³⁴, L. Danese⁷⁰, R. D. Davies⁵⁵, R. J. Davis⁵⁵, P. de Bernardis²⁴, G. de Gasperis²⁸, A. de Rosa⁴⁰, G. de Zotti^{37,70}, J. Delabrouille³, J.-M. Delouis⁴⁸, F.-X. Désert⁴³, C. Dickinson⁵⁵, S. Donzelli^{41,51}, O. Doré^{54,8}, U. Dörl⁶³, M. Douspis⁴⁷, X. Dupac³², G. Efstathiou⁵⁰, T. A. Enßlin⁶³, F. Finelli⁴⁰, O. Forni^{76,7}, M. Frailis³⁹, E. Franceschi⁴⁰, S. Galeotta³⁹, K. Ganga^{3,45}, M. Giard^{76,7}, G. Giardino³³, Y. Giraud-Héraud³, J. González-Nuevo⁷⁰, K. M. Górski^{54,80}, S. Gratton^{56,50}, A. Gregorio²⁶, I. A. Grenier⁵⁸, A. Gruppuso⁴⁰, F. K. Hansen⁵¹, D. Harrison^{50,56}, S. Henrot-Versillé⁶¹, D. Herranz⁵³, S. R. Hildebrandt^{8,60,52}, E. Hivon⁴⁸, M. Hobson⁴, W. A. Holmes⁵⁴, W. Hovest⁶³, R. J. Hoyland⁵², K. M. Huffenberger⁷⁹, T. R. Jaffe^{76,7}, A. H. Jaffe⁴⁴, W. C. Jones¹⁷, M. Juvela¹⁶, E. Keihänen¹⁶, R. Keskitalo^{54,16}, T. S. Kisner⁶², R. Kneissl^{31,5}, L. Knox²⁰, H. Kurki-Suonio^{16,35}, G. Lagache⁴⁷, A. Lähteenmäki^{1,35}, J.-M. Lamarre⁵⁷, A. Lasenby^{4,56}, R. J. Laureijs³³, C. R. Lawrence⁵⁴, S. Leach⁷⁰, R. Leonardi^{32,33,21}, C. Leroy^{47,76,7}, P. B. Lilje^{51,9}, M. Linden-Vørnle¹², M. López-Caniego⁵³, P. M. Lubin²¹, J. F. Macías-Pérez⁶⁰, C. J. MacTavish⁵⁶, B. Maffei⁵⁵, N. Mandolesi⁴⁰, R. Mann⁷¹, M. Maris³⁹, D. J. Marshall^{76,7*}, E. Martínez-González⁵³, S. Masi²⁴, S. Matarrese²³, F. Matthai⁶³, P. Mazzotta²⁸, P. McGehee⁴⁵, P. R. Meinhold²¹, A. Melchiorri²⁴, L. Mendes³², A. Mennella^{25,39}, M.-A. Miville-Deschênes^{47,6}, A. Moneti⁴⁸, L. Montier^{76,7}, G. Morgante⁴⁰, D. Mortlock⁴⁴, D. Munshi^{72,50}, A. Murphy⁶⁶, P. Naselsky^{67,29}, P. Natoli^{27,2,40}, C. B. Netterfield¹⁴, H. U. Nørgaard-Nielsen¹², F. Noviello⁴⁷, D. Novikov⁴⁴, I. Novikov⁶⁷, S. Osborne⁷⁵, F. Pajot⁴⁷, R. Paladini^{74,8}, F. Pasian³⁹, G. Patanchon³, O. Perdereau⁶¹, L. Perotto⁶⁰, F. Perrotta⁷⁰, F. Piacentini²⁴, M. Piat³, S. Plaszczynski⁶¹, E. Pointecouteau^{76,7}, G. Polenta^{2,38}, N. Ponthieu⁴⁷, T. Poutanen^{35,16,1}, G. Prézeau^{8,54}, S. Prunet⁴⁸, J.-L. Puget⁴⁷, J. P. Rachen⁶³, W. T. Reach⁷⁷, R. Rebolo^{52,30}, W. Reich⁶⁴, C. Renault⁶⁰, S. Ricciardi⁴⁰, T. Riller⁶³, I. Ristorcelli^{76,7}, G. Rocha^{54,8}, C. Rosset³, J. A. Rubiño-Martín^{52,30}, B. Rusholme⁴⁵, M. Sandri⁴⁰, D. Santos⁶⁰, G. Savini⁶⁹, D. Scott¹⁵, M. D. Seiffert^{54,8}, P. Shellard¹⁰, G. F. Smoot^{19,62,3}, J.-L. Starck^{58,11}, F. Stivoli⁴², V. Stolyarov⁴, R. Stompor³, R. Sudiwala⁷², J.-F. Sygnet⁴⁸, J. A. Tauber³³, L. Terenzi⁴⁰, L. Toffolatti¹³, M. Tomasi^{25,41}, J.-P. Torre⁴⁷, M. Tristram⁶¹, J. Tuovinen⁶⁵, G. Umana³⁶, L. Valenziano⁴⁰, J. Varis⁶⁵, P. Vielva⁵³, F. Villa⁴⁰, N. Vittorio²⁸, L. A. Wade⁵⁴, B. D. Wandelt^{48,22}, A. Wilkinson⁵⁵, N. Ysard¹⁶, D. Yvon¹¹, A. Zacchei³⁹, and A. Zonca²¹

(Affiliations can be found after the references)

ABSTRACT

Planck has observed the entire sky from 30 GHz to 857 GHz. The observed foreground emission contains contributions from different phases of the interstellar medium (ISM). We have separated the observed Galactic emission into the different gaseous components (atomic, molecular and ionised) in each of a number of Galactocentric rings. This technique provides the necessary information to study dust properties (emissivity, temperature, etc.), as well as other emission mechanisms as a function of Galactic radius. Templates are created for various Galactocentric radii using velocity information from atomic (neutral hydrogen) and molecular (¹²CO) observations. The ionised template is assumed to be traced by free-free emission as observed by *WMAP*, while 408 MHz emission is used to trace the synchrotron component. Gas emission not traced by the above templates, namely “dark gas”, as evidenced using *Planck* data, is included as an additional template, the first time such a component has been used in this way. These templates are then correlated with each of the *Planck* frequency bands, as well as with higher frequency data from *IRAS* and *DIRBE* along with radio data at 1.4 GHz. The emission per column density of the gas templates allows us to create distinct spectral energy distributions (SEDs) per Galactocentric ring and in each of the gaseous tracers from 1.4 GHz to 25 THz (12 μm). The resulting SEDs allow us to explore the contribution of various emission mechanisms to the *Planck* signal. Apart from the thermal dust and free-free emission, we have probed the Galaxy for anomalous (e.g., spinning) dust as well as synchrotron emission. We find the dust opacity in the solar neighbourhood, $\tau/N_H = 0.92 \pm 0.05 \times 10^{-25} \text{ cm}^2$ at 250 μm, with no significant variation with Galactic radius, even though the dust temperature is seen to vary from over 25 K to under 14 K. Furthermore, we show that anomalous dust emission is present in the atomic, molecular and dark gas phases throughout the Galactic disk. Anomalous emission is not clearly detected in the ionised phase, as free-free emission is seen to dominate. The derived dust properties associated with the dark gas phase are derived but do not allow us to reveal the nature of this phase. For all environments, the anomalous emission is consistent with rotation from polycyclic aromatic hydrocarbons (PAHs) and, according to our simple model, accounts for (25 ± 5)% (statistical) of the total emission at 30 GHz.

Key words. Infrared: ISM, ISM: general, Galaxy: general, Radiation mechanisms: general, Radio continuum: ISM, Submillimeter: ISM

1. Introduction

In order to understand our own Galaxy, it is necessary to explore Galactic Plane ($|b| \lesssim 10^\circ$), where we are able to observe the emission coming from a large range of distances. However the

observed emission is the sum of a large number of line-of-sight components, often probing very different environments.

Several previous studies (Bloemen et al. 1986; Bloemen et al. 1990; Giard et al. 1994; Sodroski et al. 1997; Paladini et al. 2007) have separated observed integrated emission into a number of Galactocentric radii in order to study its

* Corresponding author: douglas.marshall@cesr.fr

properties as a function of Galactic position and in different phases of the interstellar gas (e.g., atomic, molecular and ionised). The radial velocity of the gas is used to separate the Galactic gas emission into a number of Galactocentric rings and then the spectral energy distribution of each ring/gas phase is fitted with a physical model of dust and gas emissions. These methods have been used successfully in previous studies to map out basic properties of the ISM throughout the Galaxy.

For instance, Giard et al. (1994) demonstrated that polycyclic aromatic hydrocarbons (PAHs) are a ubiquitous component of the interstellar medium, and Bloemen et al. (1990) showed that the dust temperature decreases with distance to the Galactic Centre in a way which is fully consistent with an exponential decrease of the interstellar radiation field (ISRF) in the stellar disk. Sodroski et al. (1997) suggested that the abundance of large dust grains within each gas phase exhibits a gradient that is equivalent, within the uncertainties, to the metallicity gradient in the Galactic disk. Paladini et al. (2007) showed that the dust in molecular clouds appears to be heated in a significant way by young massive stars still embedded in their parent clouds.

With the advent of the *Planck* satellite¹, it is now possible to perform an inversion on the emission arising from the entire infrared, millimetre and centimetre range, making it possible to determine the dust and gas properties in many different environments in the Milky Way. The High Frequency Instrument (HFI) channels (100–857 GHz) allow us to properly constrain the big grain temperature and emissivity, while using the Low Frequency Instrument (LFI) channels (30–70 GHz), it is possible to constrain non-thermal emission mechanisms such as free-free, synchrotron or anomalous dust. We have used these data along with other ancillary data to perform a large-scale, low-resolution analysis of the Milky Way ISM emission.

Knowledge of the dust emission and physical conditions throughout the Milky Way provides a self-consistent context for other *Planck* studies: for example, the environmental effect on the properties of cold cores (Planck Collaboration 2011e,f) can be evaluated, the modelling of individual anomalous dust regions can be placed in a Galaxy-wide context (Planck Collaboration 2011d), or the Milky Way values can simply be compared to other galaxies (Planck Collaboration 2011a,b).

In Sect. 2 we describe the data used in the study, including both those to be inverted and those used as templates to represent a particular phase of the ISM. In Sect. 3, we describe how we optimise the separation of the gas observation into a number of Galactocentric rings, as well as how we report uncertainties on our best solution. We present the results in Sect. 4, and discuss potential sources of uncertainty and bias in Sect. 5. Finally we conclude in Sect. 6.

2. Data

There are two categories of data used in this study, the data to be inverted, and data used to create templates which will be used to perform the inversion.

¹ *Planck* (<http://www.esa.int/Planck>) is a project of the European Space Agency (ESA) with instruments provided by two scientific consortia funded by ESA member states (in particular the lead countries: France and Italy) with contributions from NASA (USA), and telescope reflectors provided in a collaboration between ESA and a scientific consortium led and funded by Denmark.

2.1. Data to be inverted

We use data from 12 μm (25 THz) to 1.4 GHz in order to study the dust and gas properties in a self consistent manner throughout the Milky Way. Here we briefly present these data in order of decreasing (increasing) frequency (wavelength).

The Infrared Astronomical Satellite (*IRAS*), a joint project of the US, UK, and the Netherlands (Neugebauer et al. 1984), performed a survey of 98% of the sky at four wavelengths: 12, 25, 60, and 100 μm . We use a reprocessed version of this data set (IRIS, Miville-Deschênes & Lagache 2005) which benefits from a better zodiacal light subtraction and from a calibration and zero level compatible with DIRBE, as well as from a better destriping.

The DIRBE instrument (Diffuse Infrared Background Experiment, Hauser et al. 1998) on board the *COBE* satellite imaged the full sky in 10 broad photometric bands from 1 to 240 μm with a beam of 0.7°. The bands at 140 and 240 μm allow us to bridge the gap between *IRAS* and the highest frequencies of HFI, thus covering the peak of the thermal dust spectral energy distribution (SED).

The *Planck* data we used for this analysis are the DR2 LFI and HFI maps, with the cosmic microwave background (CMB) removed, as described in detail in Zacchei, A., Maino, D., Baccigalupi, C. et al. (2011) and Planck HFI Core Team (2011), respectively. It consists of a set of 9 frequency maps with central frequencies of 28.5, 44.1, 70.3, 100, 143, 217, 353, 545 and 857 GHz, smoothed to a common resolution of 1° FWHM, at a common HEALPix (Górski et al. 2005) pixelization resolution of $N_{\text{side}}=256$ ($\sim 15'$ pixels). For simplicity, in the remainder of the text we will refer to the first three bands as 30, 44 and 70 GHz, respectively. The CMB component that was removed from these maps was found by the Needlet Internal Linear Combination (NILC) CMB extraction method presented in Planck HFI Core Team (2011).

Finally, to provide constraints at radio frequencies we use the full-sky 1.4 GHz data from (Reich 1982; Reich & Reich 1986; Reich et al. 2001).

All of the above data sets have been smoothed with a Gaussian function to a common resolution of 1° FWHM and gridded to a common HEALPix N_{side} of 256.

2.2. Templates

2.2.1. Atomic phase

We aim to characterise the different emission mechanisms in the different phases of the interstellar medium (atomic, molecular and ionised). For the atomic phase we use the Leiden/Argentine/Bonn Galactic H I Survey (Kalberla et al. 2005). The survey results are expressed in antenna temperature, T_A . In order to convert this into column density, the effect of optical depth should be taken into account, for example (Binney & Merrifield 1998)

$$N_{\text{HI}} = 1.82 \times 10^{-18} \times \int_{\nu_1}^{\nu_2} T_s \times \ln \left(1 - \frac{T_A}{T_s} \right)^{-1} d\nu \text{ cm}^{-2}, \quad (1)$$

for a given spin temperature (T_s). Recent studies in the plane of the Milky Way (Dickey et al. 2003, 2009) advocate the use of a higher spin temperature of around 250 K. This higher value is justified on the grounds that along any line of sight there is a mix of cold and warm H I gas, and so an effective spin temperature is needed to correct for the opacity. This will most certainly vary as a function of Galactic longitude. However, constraining this

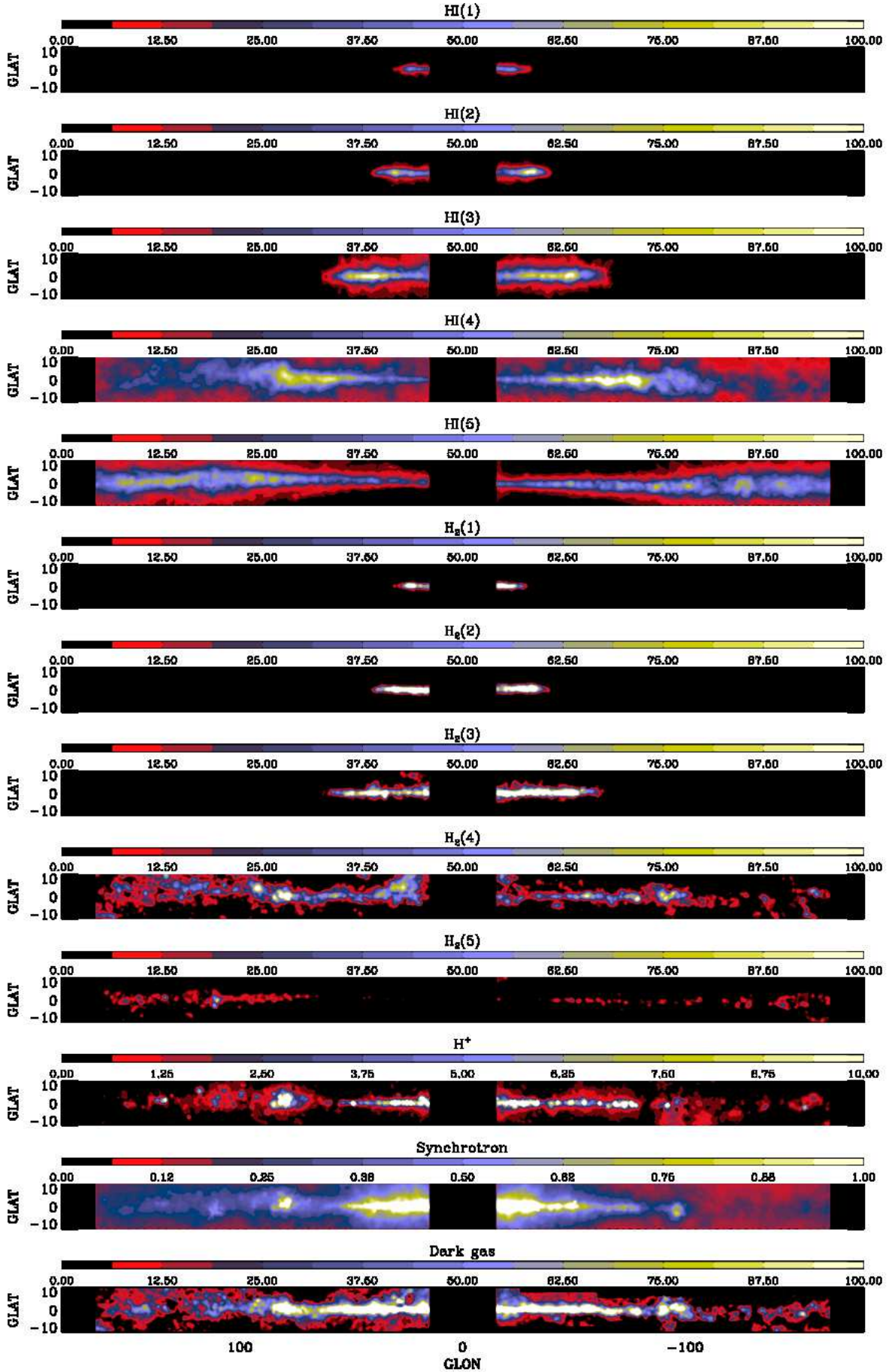


Fig. 1. Templates used in the inversion. The top five images are the HI templates, the following five are the molecular templates, all of which are presented in increasing Galactocentric radius (the radii defining each ring are described in Sect. 3.2). The final three templates are the free-free, synchrotron, and dark gas templates, respectively. The units are all expressed in 10^{20} atoms, except for synchrotron, expressed in MJy sr^{-1} . The centre and anti-centre regions have been masked as no distance information can be obtained from the radial velocity of the gas.

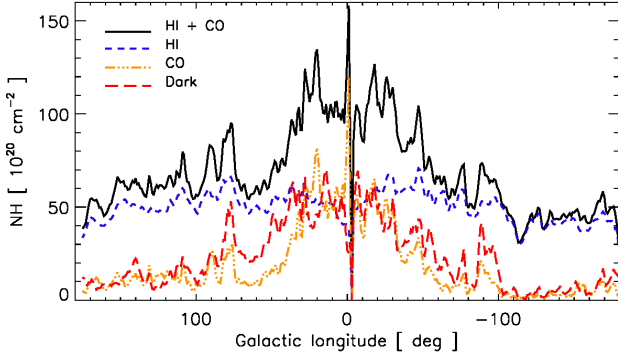


Fig. 2. Longitude profile of H I, CO and dark gas. The black solid line shows the total contribution from H I & CO. The dark gas represents a significant fraction of the gas column density, and dominates the CO outside of the molecular ring.

variation is beyond the scope of this study. We have therefore assumed a constant hydrogen spin temperature of 250 K for the entire Galactic Plane. Varying this value in the range 150–400 K has only a small effect on our results and they remain consistent within the quoted uncertainties.

2.2.2. Molecular phase

We assume that the bulk of the molecular gas mass is at first order well traced by CO emission (Tielens 2005). The CO data we use come from the Composite CO Survey of Dame et al. (2001). The column density of molecular hydrogen can be expressed as a function of antenna temperature (T_{CO})

$$N_{\text{H}_2} = 2 \times X_{\text{CO}} \times \int_{v_1}^{v_2} T_{\text{CO}} dv. \quad (2)$$

where $X_{\text{CO}} = N(\text{H}_2)/W_{\text{CO}}$ is the ratio of molecular hydrogen column density to the velocity-integrated intensity of the ^{12}CO line. We use a value for X_{CO} which is compatible with the recent values from the *FERMI* collaboration (Abdo et al. 2010; Ackermann et al. 2011), $X_{\text{CO}} = 1.8 \times 10^{20}$, which results from a study on diffuse gamma-ray emission in the Galactic plane.

Both the atomic and molecular data contain line of sight velocity information. It is therefore possible to use this information to separate the emission into a set of Galactocentric rings, as a given line of sight velocity measurement uniquely identifies a Galactocentric distance, assuming circular orbits. This should not be confused with heliocentric distances for which there is a distance ambiguity corresponding to the near or far side of the derived Galactocentric orbit. The velocity information alone does not allow one to determine if the observed gas is on the near side of the determined orbit or on the far side. We separate the observed H I and CO observations each into a set of 5 Galactocentric rings. The reasons for choosing this decomposition is explained in Sect. 3.2

2.2.3. Dark gas

It has been shown (e.g., Reach et al. 1994; Grenier et al. 2005) that the CO and H I do not account for all the atomic and molecular gas in interstellar clouds: there is in addition a dark gas phase. This phase is also extensively studied in Planck Collaboration (2011c), where the total gas column density, as traced by H I and CO observations, is correlated with the optical depth of the dust

calculated using *IRAS* $100\ \mu\text{m}$ along with *Planck* HFI data at 350 and $500\ \mu\text{m}$ (857 and 545 GHz). The correlation is linear at low and high column densities, but it departs from linearity at column densities of $7.4 \times 10^{20} < N_{\text{H}} < 5.0 \times 10^{21}$. This excess is attributed to thermal emission by dust associated with a dark gas phase, undetected by H I and CO measurements.

The dark gas column density used here is defined in Planck Collaboration (2011c) as

$$N_{\text{H}}^{\text{X}} = (\tau_{\text{D}} - \tau_{\text{M}}) / \left(\frac{\tau_{\text{D}}}{N_{\text{H}}} \right)^{\text{ref}}, \quad (3)$$

where τ_{D} is the thermal dust optical depth, $\tau_{\text{M}} = (\tau_{\text{D}}/N_{\text{H}})^{\text{ref}} [N_{\text{H}} + 2X_{\text{CO}}W_{\text{CO}}]$ is the modelled dust opacity and $(\tau_{\text{D}}/N_{\text{H}})^{\text{ref}}$ is the reference dust emissivity measured in low N_{H} regions. We use their dark gas estimate at 857 GHz as an additional template.

The dark gas phase represents a significant fraction of the total gas column density, as shown in Fig. 2. The H I dominates over almost the entire longitude range, and the CO is strongest in the molecular ring $40^\circ > l > -40^\circ$. Outside of the molecular ring the dark gas is stronger than the CO, except towards the anti-centre direction where the dark gas and CO are roughly comparable. The proportion of dark gas to total hydrogen column density ranges from roughly 10% in the anti-centre direction up to nearly 60% towards the Galactic centre.

2.2.4. Synchrotron emission

An additional emission mechanism which is important in the frequency range we are studying and is not traced by usual gas tracers is synchrotron emission, which arises from the acceleration of cosmic-ray electrons in magnetic fields. This emission follows approximately a power law but the spectral index most certainly varies on the sky and as a function of frequency. More than 90% of the observed synchrotron emission arises from a diffuse component (Bennett et al. 2003) and in the Galactic plane recent studies have shown that there is no hardening of the synchrotron spectrum (Finkbeiner 2004; Boughn & Pober 2007), but that emission from spinning dust is likely to dominate between 8 and 60 GHz. For our synchrotron template we have chosen the 408 MHz all-sky survey from Haslam et al. (1982), which traces the diffuse, soft synchrotron component.

2.2.5. Ionised phase

To represent the ionised component we have used the Maximum Entropy Method (MEM) free-free template from the *WMAP* seven year data (Jarosik et al. 2011). The intensity map (I_{ν}) has been converted to ionised hydrogen column density as described by Sodroski et al. (1997):

$$N_{\text{HII}} = 1.2 \times 10^{15} T_{\text{e}}^{0.35} \nu^{0.1} n_{\text{eff}}^{-1} I_{\nu} \quad (4)$$

for effective electron density n_{eff} and electron temperature T_{e} . Following Sodroski et al. (1989), we use $n_{\text{eff}} = 10\ \text{cm}^{-3}$ and $T_{\text{e}} = 8000\ \text{K}$. In the future, the availability of radio recombination line (RRL) surveys will provide a more direct measurement of the free-free component in the Galaxy and its distribution separated into distinct Galactocentric bins using the radial velocity information included in such surveys.

As has been done for the data, the templates have all been smoothed to 1° FWHM and gridded to an N_{side} of 256. These templates are all displayed in Fig. 1.

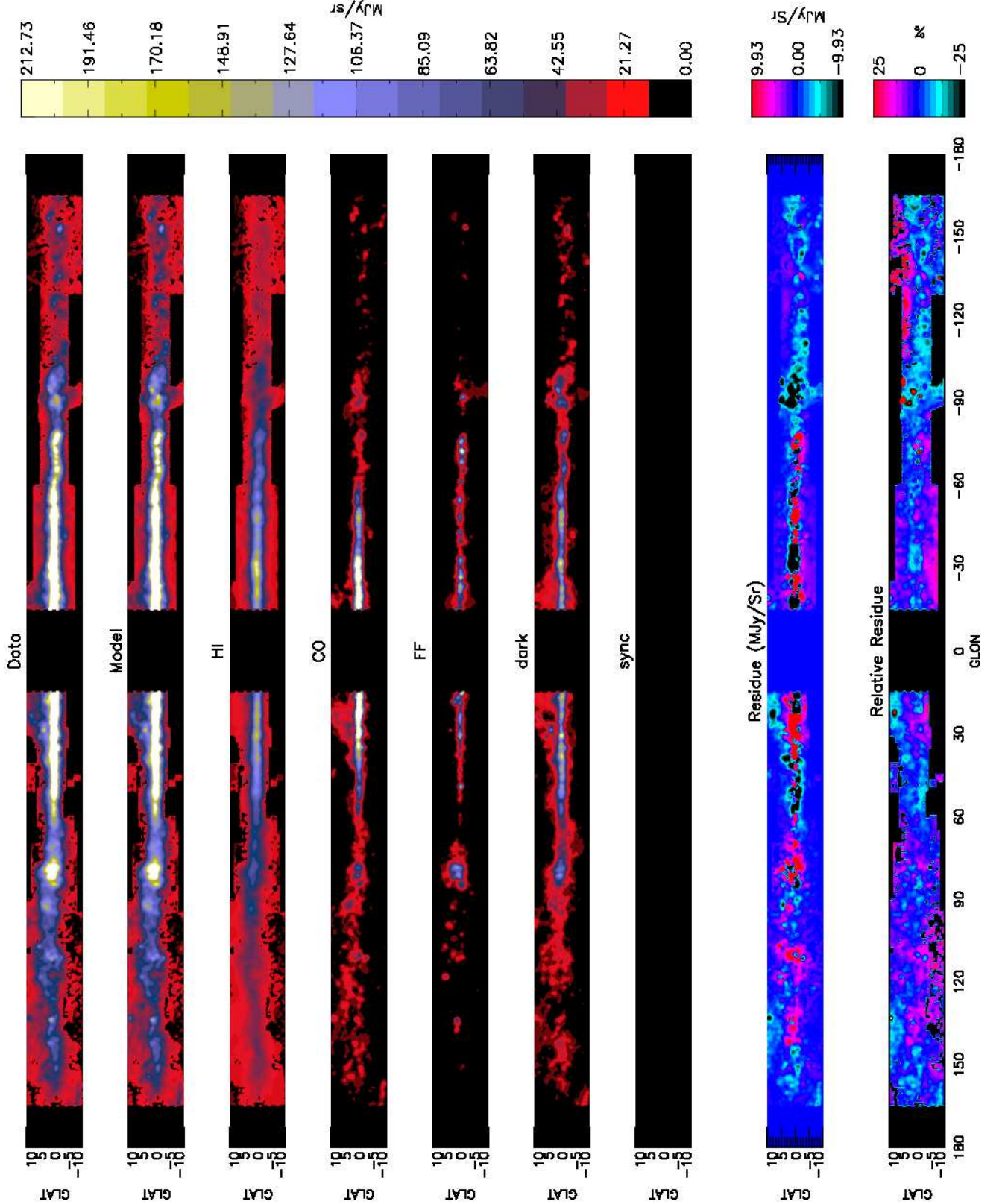


Fig. 3. Results of the inversion for the 857 GHz band. From top to bottom are: observed emission; modelled emission; atomic contribution; molecular contribution; ionised contribution; dark gas contribution; synchrotron contribution; residual; and relative residual. All images except for the residual maps are at the same intensity scale. The centre and anti-centre regions have been masked, as the kinematic distance method is inapplicable to these regions. Areas where no CO observations are available have also been masked.

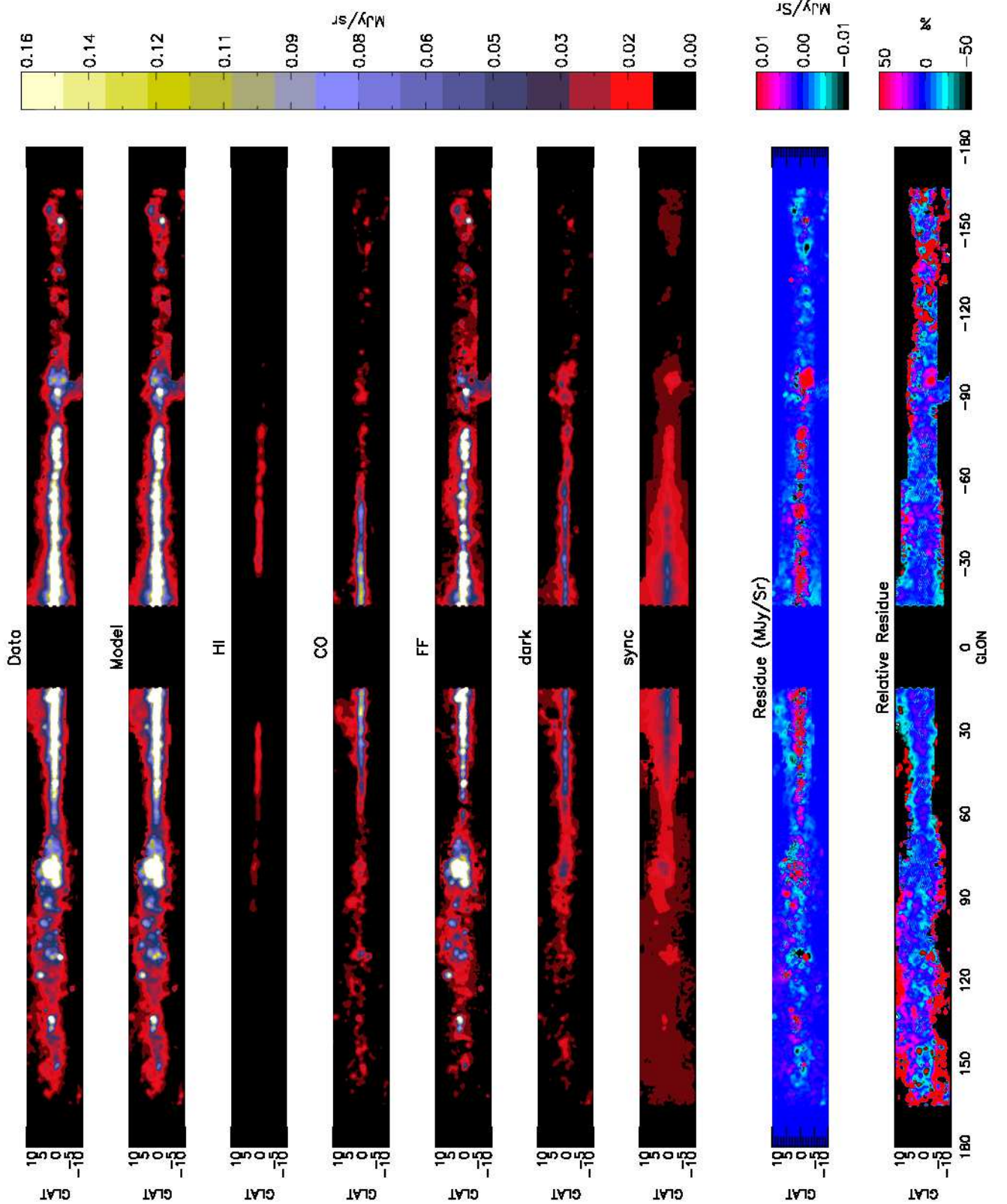


Fig. 4. Same as Fig. 3 for the 30 GHz band.

3. The Galactic inversion

Component separation techniques have been widely tested in the framework of multi-frequency observations of the CMB, espe-

cially in the context of *Planck* (see Leach et al. 2008, , for a review of the methods developed within the *Planck* collaboration). These methods exploit spectral and spatial correlations and independence in observations made at separate frequencies, as well

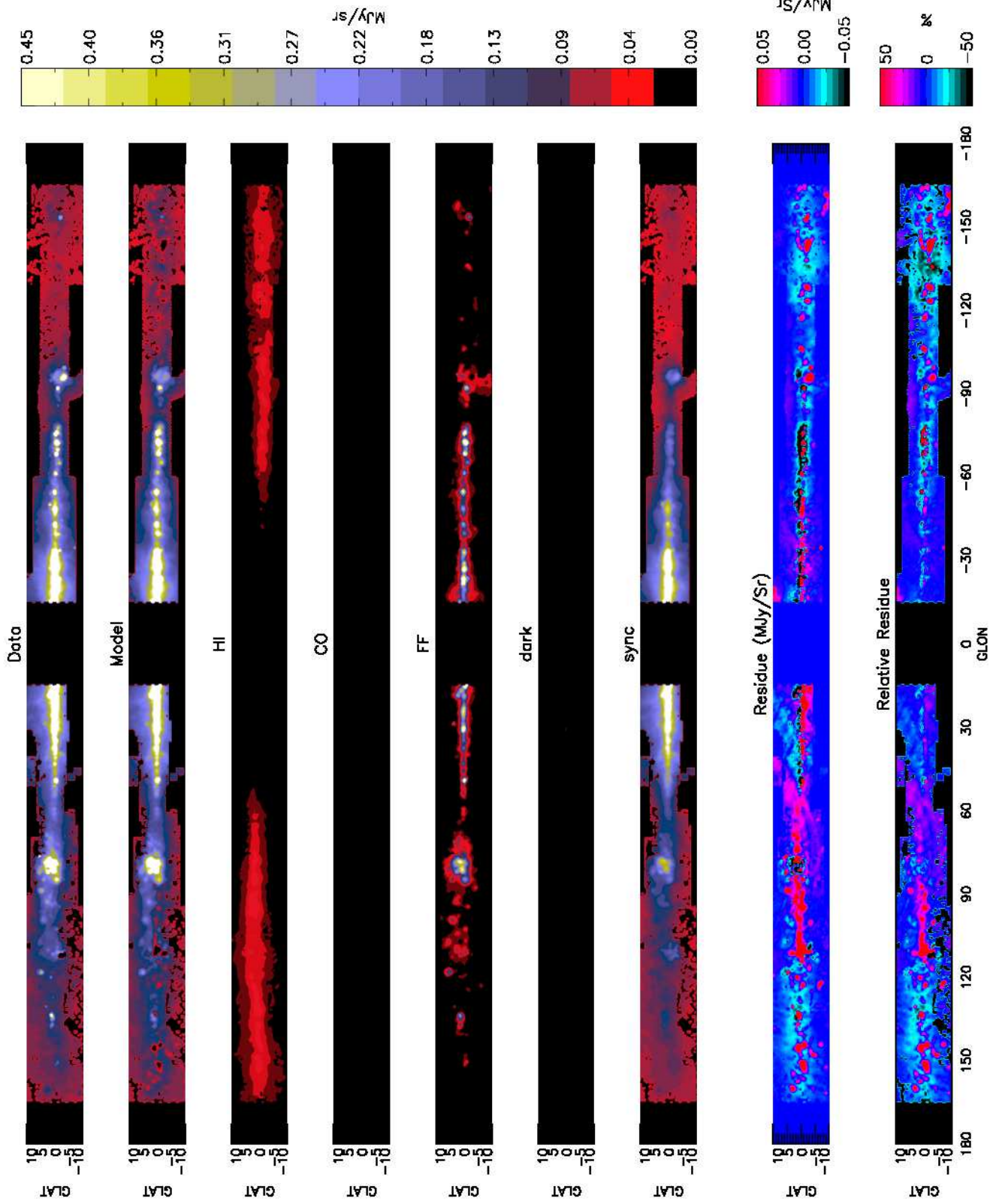


Fig. 5. Same as Fig. 3 for the 1.4 GHz band.

as external constraints and physical modelling, in order to distinguish between different physical sources of emission. Most of them are designed to efficiently separate CMB from foregrounds and possibly foregrounds into “components”: (Galactic

synchrotron, free-free and dust emissions; extra-galactic and far-IR point sources; Sunyaev-Zeldovich effect, etc.

The approach presented here is different from these methods as it tries to quantify the separate components responsible for

diffuse Galactic emission. Nevertheless it is not strictly speaking a component separation method, in the sense presented above, as it fits one map of the sky with spatial templates at different Galactocentric distances and is not exploiting the spectral signature of each component to perform the separation.

3.1. Inversion method

We assume that each of the frequency maps (I_ν) can be expressed as a linear combination of the spatial templates described in Sect. 2.2 and presented in Fig. 1. Then, for each frequency map, we are solving for the mean emissivity of each template (in units of MJy sr⁻¹ / 10²⁰atoms) which best reproduces the observed data. Note that we are not taking into account any spatial variations of the emissivity within a given template, but are assuming a constant value for each of our templates. The modelled emission can be written, for any frequency map $I_\nu(x, y)$, as:

$$I_\nu^m(x, y) = \sum_{i=1}^n \left(\epsilon_{\text{H I}}^i(\nu) N_{\text{H I}}^i(x, y) + \epsilon_{\text{H}_2}^i(\nu) N_{\text{H}_2}^i(x, y) \right) + \epsilon_{\text{H II}}(\nu) N_{\text{H II}}(x, y) + \epsilon_s(\nu) N_s(x, y) + \epsilon_d(\nu) N_d(x, y) + C_\nu, \quad (5)$$

where the sum is over a number (n) of Galactocentric rings (i) for the atomic and molecular phases, denoted $N_{\text{H I}}$ and N_{H_2} respectively. $N_{\text{H II}}$, N_s and N_d denote the ionised, synchrotron and dark gas components, respectively, and C_ν is a constant. Note that the last three templates do not have any rings, as we have no way of separating the information into different Galactocentric distances and so they are a function of frequency only. As such, the quoted ϵ are a function of ν only.

In order to find the values for the different emissivities, ϵ , we minimise the chi-squared value defined by

$$\chi^2 = \sum_{j=1}^{N_{\text{pixels}}} \frac{(I_{\text{mod}}(j)_\nu - I(j)_\nu)^2}{\sigma_\nu^2}, \quad (6)$$

where σ_ν is the noise in the map I_ν , estimated as the median value of the intensity for $|b| > 70^\circ$.

In our case, the difference between model and observations is not at all dominated by the low noise present in the *Planck* bands, but by the simplistic model that we are adopting for the inversion. As such we suppose that the noise does not vary spatially.

The solution which minimises Eq. 6 is found via matrix inversion. By writing the problem as

$$b_i = a_j \cdot A_{ij}, \quad (7)$$

where b is the observed intensity map, A is an $N \times M$ matrix of the different templates and a is the vector of the parameters. The solution is simply (Press et al. 1992)

$$a = (A^T A)^{-1} \times A^T b. \quad (8)$$

The optimal mathematical solution which solves Eqs. 5–6 may not be physical; in particular, it may include negative emissivities. However, we do not have any cases where the emissivity is more than one sigma below zero, so remaining consistent with zero. As such we do not place any constraints on the parameters of the inversion.

3.2. Galactocentric ring optimisation

The observed radial velocities of H I and CO are used to separate the observed emission into a number of Galactocentric rings,

assuming circular orbits for the gas and using the rotation curve from Clemens (1985). The choice of the distance intervals for the rings is not arbitrary, but is subject to a number of constraints. Choosing too many would create a set of rings that would be highly correlated and result in a degenerate solution. An optimised set of rings has been defined by minimising the correlation between rings, and thus minimising the degeneracy between the various components of the inversion. The total number of rings and their thickness are also driven by the requirement of a minimal number of data falling into each ring in order to constrain it and separate its contribution from the others. Further, we have chosen to fix the solar circle as one of the rings, including all velocity channels that contain high latitude, low velocity clouds.

The ring optimisation process consists first in dividing the H I and CO templates into a large number of small rings, and then building the covariance matrix ($A^T A$, see Eq. 8) associated with this highly discrete basis of annuli. An iterative process is then performed: neighbouring rings with the highest correlation are merged and the new covariance matrix is updated with a reduced number of annuli. The process continues, merging the rings which have strongest correlation between them, until a reasonable number of rings is obtained. This leads to the following decomposition: $R_{\text{GAL}} = [1.5, 4.2, 5.4, 7.1, 9.8, 25.0]$ kpc, where the values define the ring edges.

3.3. Estimating uncertainty

The result of the inversion is an average gas emissivity at each frequency, in each gas phase and in each ring (when available). However, within a given gas phase the dust and gas properties may vary significantly and we wish to report this uncertainty. In other words, the residual differences between the model and the data are not due to noise in the data, meaning that the uncertainty on the resulting emissivities cannot be computed analytically (i.e., the residuals are not well-modelled by the uniform Gaussian noise implicit in the solution, Eq. 8). The residuals are rather due to unknown differences between the templates and the data. An alternate method is then needed to estimate the uncertainties on the results.

The dust properties in the northern Galaxy may differ from those in the southern part, and of course the variation may be even more localised than that. To quantify this uncertainty we perform jackknife tests by masking approximately 30% of the Galaxy in 30 random blocks, each 3° wide, and performing the inversion on the unmasked zones. This is repeated 500 times, and the rms value of the jackknife tests is used to provide the total variation of the emissivity within each ring and gas phase. We therefore provide robust estimates of the dust emission and provide their variation for each ring and gas phase.

It should be stressed that this estimation does not take into account the errors on either the H I opacity correction nor the uncertainty on the assumed X_{CO} value for each phase globally.

4. Properties of the ISM in the Galactic plane

The above inversion method has been applied to 16 different frequency bands from 12 μm (25 THz) to 1.4 GHz. The results are presented in table form in the appendix (Table A.1).

Figures 3, 4 and 5 compare our best-fit model to the data for three frequencies (two *Planck* frequencies, 857 and 30 GHz, as well as the 1.4 GHz radio frequency) and the contributions of the different gas components to the model. The model reproduces the data rather well, especially when one notices the scale of the

residual. The contours in the relative residual are drawn every 25%, so nearly the full zone used in the inversion has residuals below this level.

The main contributors to the 857 GHz map (see Fig. 3) are the atomic and molecular phases (including the dark gas) with a modest contribution from the ionised component. At 30 GHz (Fig. 4) the emission is a combination of the molecular, ionised, dark gas and synchrotron, with very little hydrogen. As for the solution at 1.4 GHz (Fig. 5) it is the synchrotron component that dominates the solution, but with a significant contribution from the ionised component.

4.1. Dust in thermal equilibrium

We have constructed SEDs for each of our templates across all frequencies that we have analysed. Where the emissivity is compatible with zero, we plot the 2σ upper limit as a downward arrow.

We have fit the SEDs using a sum of thermal dust (big grains), spinning PAH molecules, free-free and synchrotron emission. The large dust grains in thermal equilibrium are well described by a modified blackbody of the form

$$I_\nu \propto B_\nu \frac{\nu^\beta}{\nu_0} = \frac{2h\nu^3}{c^2(e^{h\nu/kT} - 1)} \frac{\nu^\beta}{\nu_0}, \quad (9)$$

where T is the dust temperature and β is the emissivity spectral index. When fitting using both T and β as free parameters, we find a mean value of $\beta = 1.8 \pm 0.1$ throughout the Galaxy. However, to increase the reliability of the fit, we follow Planck Collaboration (2011g,h,c) and fix $\beta = 1.8$. We use all data points down to 143 GHz in the fit, but exclude 217 GHz in the molecular and dark gas phases due to contamination from CO line emission. All points are colour corrected assuming $\nu I_\nu = \text{constant}$ as described in Planck HFI Core Team (2011). The SEDs for the atomic, molecular and ionised phases are shown in Figs. 6, 7 and 8, respectively. We are able to constrain the dust temperature for each component and in the various Galactocentric radii. The resulting temperature profile is shown in Fig 9. The temperature in the atomic phase is seen to decline steadily with increasing Galactocentric distance. This decrease in temperature follows the trend of the ambient ISRF (Mathis et al. 1983), shown by the solid line in Fig 9, indicating that the dust in the atomic phase is predominantly heated by it.

The dust in the molecular component, however, is seen to be more steady, peaking in the molecular ring ($3 \lesssim R_G \lesssim 6$ kpc) and once again outside the solar circle. This phase seems to be heated by the presence of star formation. The ionised phase (dotted line) is seen to be dominated by grains that are on average much warmer than either of the other two phases. These results are in agreement with previous Galactic analyses (Sodroski et al. 1997; Paladini et al. 2007). The temperature within the solar circle ($T = 17.6 \pm 0.1$ K) is completely in agreement with the average value at high Galactic latitude (Planck Collaboration 2011g).

The dust opacity at a given wavelength is defined as τ_λ/N_H where $\tau_\lambda = \epsilon_\lambda/B(\nu, T)$ is the dust optical depth. The dust opacity in the atomic phase for the solar circle is equal to $0.92 \pm 0.05 \times 10^{-25} \text{ cm}^2$ at $250 \mu\text{m}$, slightly below, but in agreement with, the same value found by Planck Collaboration (2011g) at high Galactic latitude. The variation of the opacity as a function of Galactic radius is shown in Fig. 10. We do not detect any significant variation of the dust opacity as a function of Galactic radius, in either the atomic or molecular phases. Note, however,

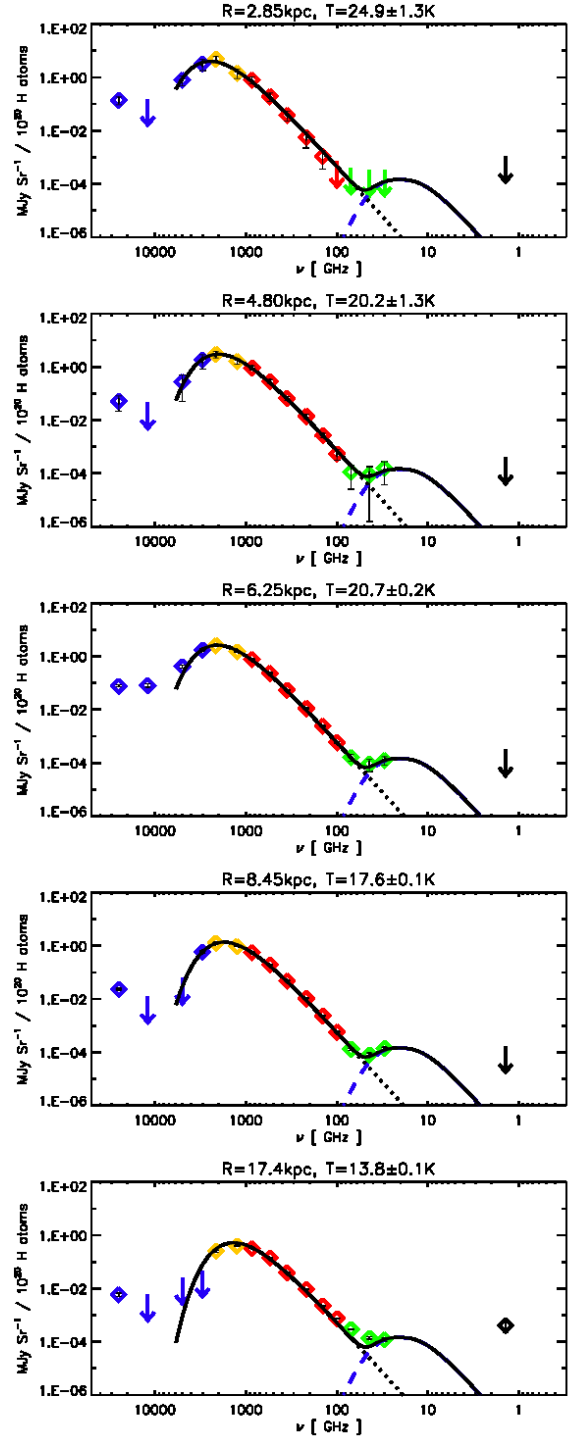


Fig. 6. SEDs for the atomic component, each sorted in increasing Galactocentric radius. The colour of the symbols refer to the mission the data came from: *IRAS* (blue), *DIRBE* (yellow), *HFI* (red), *LFI* (green) and 1.4 GHz (black). The SEDs also show various fitted laws: the dotted line is the thermal dust SED, the short dashed line spinning dust in an atomic medium, and the solid line the sum of all contributions. The spinning dust contribution is not a fit, but simply the result of using typical values in the model (see Sect. 4.2.3 for details). The contribution of the atomic component in the outer Galaxy to the 1.4 GHz signal is lower than the noise level derived for the 1.4 GHz map and so should not be viewed as significant.

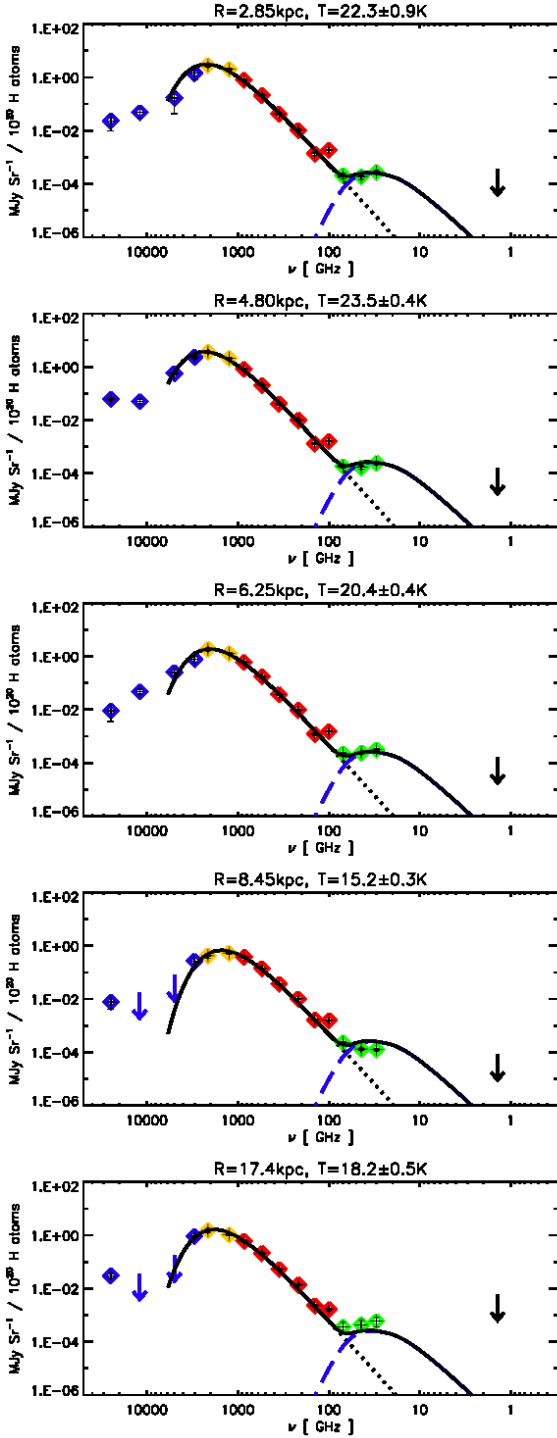


Fig. 7. SEDs for the CO component, each sorted in increasing Galactocentric radius. The different lines and colours are as described in Fig. 6, except for the long dashed line which represents spinning dust in a molecular medium.

that the opacity of the molecular component is completely degenerate with the chosen value for X_{CO} . By increasing X_{CO} , we decrease the opacity. Further, the appropriate spin temperature for the H I opacity correction may differ from the constant 250 K we have assumed.

Finally, after fitting the thermal dust in the molecular phase, there is an obvious excess at 100 and 217 GHz due to the presence of CO line emission in these *Planck* bands

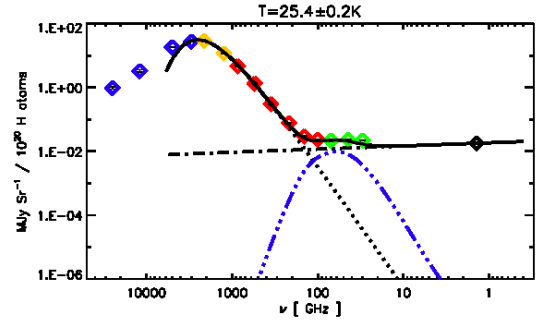


Fig. 8. The resulting SEDs for the free-free component. The different lines and colours are as described in Fig. 6, except for the dash-dot line and the dash triple dot line which represent free-free emission and spinning dust in an ionised medium, respectively.

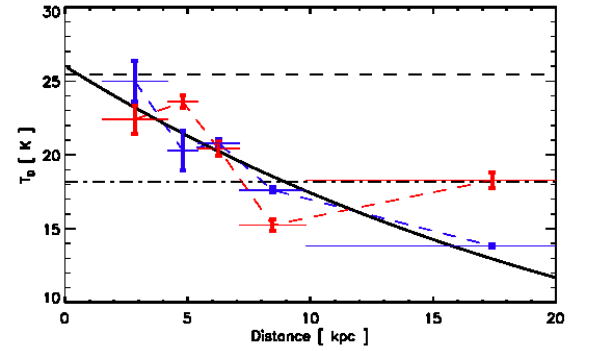


Fig. 9. Average dust temperature as a function of Galactocentric radius for the atomic (blue) and molecular (red) components. The dust temperature in the ionised phase and the dark gas phase are shown by the dashed line and dot-dashed line, respectively. The solid line shows the behaviour of the ISRF with Galactic radius. Horizontal bars show the range in distance over which the mean temperature applies. The temperature of dust mixed with atomic H I decreases with radius, consistent with the fact that this component is heated by the ambient ISRF. Dust in the molecular component is heated by embedded star formation.

(Planck HFI Core Team 2011). This is a clear indication that the inversion is working as it should, as this excess is present in the molecular phase. The excess with respect to the fit is 16.2 ± 1.0 and $20.2 \pm 4.5 \mu\text{K}_{\text{CMB}}/\text{K}_{\text{RJ}} \text{ km s}^{-1}$ at 100 and 217 GHz, respectively. Planck HFI Core Team (2011) find 14.2 ± 1.0 and 44.2 ± 6.0 at 100 and 217 GHz, respectively. At 100 GHz our value is slightly higher, which is to be expected as it is simply an excess with respect to ^{12}CO and does not take into account the other CO isotopes present along the line of sight. The difference in the values at 217 GHz is not as easy to understand, but may come from our simple assumption of a fixed β .

4.2. Analysis of non-thermal SED components

The SEDs for all components at frequencies lower than 100 GHz show non-thermal dust emission features. The emission mechanisms at work in this spectral range are thermal bremsstrahlung (free-free), synchrotron emission, as well as a third commonly referred to as anomalous dust emission.

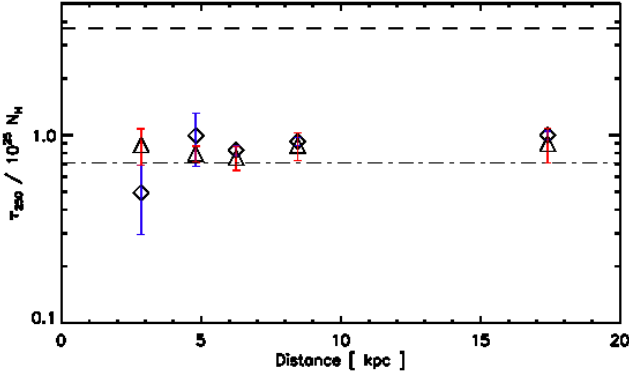


Fig. 10. Dust opacity at $250\,\mu\text{m}$ as a function of Galactocentric radii for H I (blue, diamonds) and CO (red, triangles). The dashed line and the dash dot line show the dust opacity for the ionised phase and the dark gas phase, respectively.

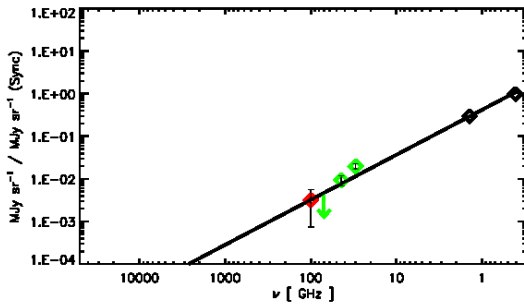


Fig. 11. The resulting SEDs for synchrotron component. The different lines and colours are as described in Fig. 6. The point at 408 MHz is not part of the inversion, but has been plotted here to show consistency.

4.2.1. Synchrotron

The SED for the synchrotron component resulting from our inversion is shown in Fig. 11. A power-law has been recovered in the two lowest frequency LFI points and the 1.4 GHz radio point.

For electrons with a power-law distribution of energies $N(E) \propto E^{-p}$ the frequency dependence of the emission is characterised by antenna temperature $T(\nu) \propto \nu^\beta$ with spectral index $\beta = -(p+3)/2$, with typically $\beta \sim -3$. As we are not working in antenna temperature, but flux density, the power law takes the form $I_\nu \propto \nu^\alpha$ with $\alpha = \beta - 2$.

We have performed a fit of the rising synchrotron spectrum with a power law and obtained a spectral index $\alpha = -1.0 \pm 0.1$. This value is slightly flatter than the average value found between 408 MHz and 23 GHz by *WMAP* (Dunkley et al. 2009; Davies et al. 2006). However, this value falls within the range of values found in the Galaxy (Bennett et al. 2003, $-0.5 < \alpha < -1.1$), and most likely represents the stronger power injection in the Galactic plane. There is no evidence in the data for any hardening of the synchrotron spectrum below 70 GHz.

4.2.2. Free-free

Free-free emission dominates the ionised hydrogen template (Fig 8) at frequencies below 143 GHz. This emission follows a power-law with a spectral index of $\alpha = -0.1$ for $70\,\text{GHz} < \nu < 1.4\,\text{GHz}$. As we have used the *WMAP* free-free template to

trace the ionised medium, it is interesting to compare the total free-free emission that we attribute to this phase with the *WMAP* estimate. Using the power-law fit shown in Fig. 8, we can extrapolate to the frequency of our choice and, using our H+ template, produce an estimate of the free-free emission in any of the *WMAP* bands.

Performing this at 23 GHz, we recover $\sim 80\%$ of the emission that the *WMAP* team find in their MEM free-free component separation. Using radio recombination lines (RRLs) from the H I Parkes Zone of Avoidance (ZOA) survey, Alves et al. (2010) recently showed that diffuse ionised emission can be recovered in the Galactic plane using RRL surveys. They then compared the level of free-free derived with the *WMAP* MEM estimate. As in this work, they showed it to be too high in the Galactic plane by at least 10%, albeit in a much smaller ($8^\circ \times 8^\circ$) region.

Looking at the molecular SEDs (Fig. 7), and the dark gas SED (Fig. 13), the LFI points depart from the thermal dust and seem to describe a free-free spectrum. It is not possible, however, to describe the three LFI points *and* the radio point using a free-free power law, except for the first and last molecular templates. Even so, all the radio points in the molecular templates are upper limits and the predicted free-free spectrum would be above the $4\text{-}\sigma$ level for three of the templates, showing that the data are not compatible with this model. In addition, if this were indeed free-free emission, our estimate of the total Galactic free-free emission would surpass that of the *WMAP* MEM free-free estimate by over 30%. This seems unlikely in light of the Alves et al. (2010) finding discussed above. In that case, the LFI-radio points in the atomic, molecular and the dark gas phases are anomalous microwave emission. Indeed, Boughn & Pober (2007) recently showed that the dominant emission mechanism at 20 GHz is spinning dust, and so is identified as anomalous microwave emission.

4.2.3. Anomalous microwave emission

Anomalous microwave emission, arising between 10 and 100 GHz and first detected in the 1990s (Kogut et al. 1996), cannot be explained using classical emission mechanisms known in this frequency range (Banday et al. 2003). Indeed it is too bright to be free-free emission, and it is not polarised as thermal dust or synchrotron emissions would be. However, it is correlated with dust IR emission and especially with the interstellar PAH and very-small-grain (VSG) emission in the mid-IR (Casassus et al. 2006; Ysard et al. 2010; Scaife et al. 2010). Anomalous emission was first proposed by Draine & Lazarian (1998) to come from rapidly rotating PAHs (Rouan et al. 1992), the spinning dust grains. Since, it has been observed in various interstellar environments: dark clouds (Watson et al. 2005; Casassus et al. 2006; Scaife et al. 2009; Dickinson et al. 2010); H II regions (Dickinson et al. 2007; Scaife et al. 2008); planetary nebulae (Casassus et al. 2007) and diffuse interstellar medium (Miville-Deschênes et al. 2008). Several processes can excite or damp the grains' rotation: photon emission (IR and radio); gas/grain interactions; formation of H₂ molecules on the grain surface; or photoelectric emission.

Here we investigate the anomalous component in CO-correlated emission. All the rings exhibit a flattening of the SED in the three LFI bands (Fig. 7), as well as upper limits on the emission at 1.4 GHz. This clear excess in the microwave range cannot be free-free emission due to the reasons discussed in Sect. 4.2.2. The peak frequency of this excess lies approximately from 20 to 60 GHz.

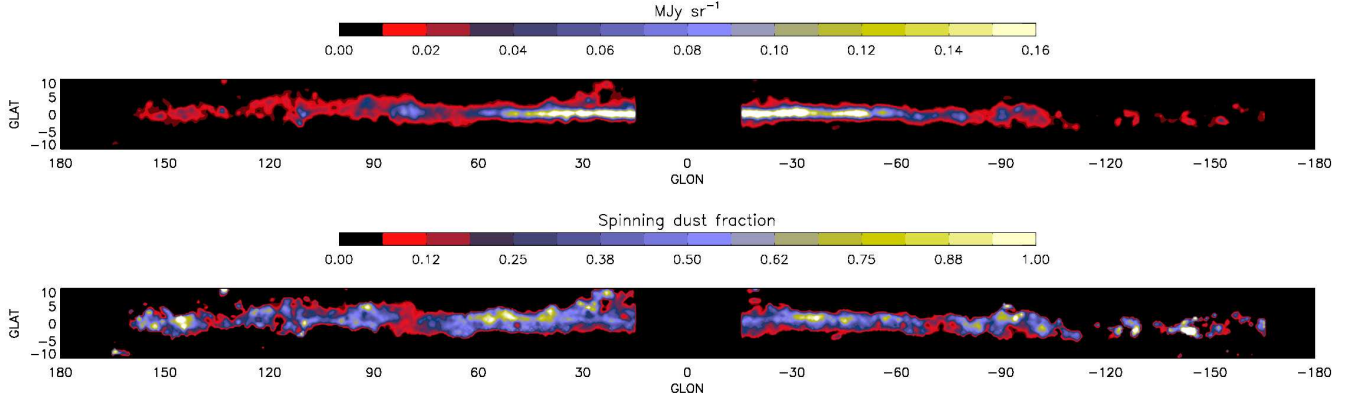


Fig. 12. Depiction of the spinning dust emission at 30 GHz in the Galactic plane in MJy sr⁻¹ (top) and as a fraction of the total 30 GHz signal (bottom). In making this image, it is assumed that the 30 GHz emission associated with the atomic, molecular and dark gas phases are solely due to spinning dust. Some features may be simply due to residuals in our inversion; however, this illustrative view highlights regions where spinning dust may be particularly strong compared to other emission mechanisms.

We attempt to fit the excess with the spinning dust model described in Silsbee et al. (2011). Models show that spinning dust emission is sensitive to the grain size distribution, to the intensity of the ISRF, and to the density of the medium in which the grains are embedded (Ali-Haïmoud et al. 2009; Ysard & Verstraete 2010). The smallest grains, namely the PAHs, are responsible for most of the spinning dust emissivity. Fitting the thermal dust emission with a modified blackbody, we estimate the radiation field to be close to the standard ISRF (Mathis et al. 1983; Porter et al. 2008). To describe the small dust grains, we use two grain populations: PAHs and VSGs. We adopt a size distribution that is the sum of two log-normal components (Weingartner & Draine 2001). The first one is peaked at 3 nm (VSG), and the second one at 0.6 nm (PAHs), in line with Compiègne et al. (2011), with the width of both log-normal components set to 0.4. Most of the spinning dust emission comes from the smallest grains, the second log-normal component, for which we assume an abundance equal to the value measured in the solar neighbourhood. Finally we describe the grains' environment as molecular gas with typical parameters ($n_H = 350$ cm⁻³ and $T_{\text{gas}} = 20$ K).

The fit to the data with this simple model is surprisingly good, and shows that not only is anomalous emission present in the molecular phase throughout the Milky Way, but that spinning dust provides a compelling model with which to describe it. The predominance of spinning dust in the molecular phase is in agreement with more detailed modelling of individual anomalous emission regions (Planck Collaboration 2011d).

The ISRF could in theory also have an effect on this emission mechanism, and the big grain temperature gives us an idea of its fluctuations: $\chi = (T/17.5\text{K})^{\beta+4}$, where χ is dimensionless and equal to one in the solar neighbourhood. However this range of ISRF fluctuations has little effect on the spinning dust spectrum (Ali-Haïmoud et al. 2009; Ysard & Verstraete 2010), so we assume a solar value for all SEDs. The average density of the molecular gas may vary with radius, which would have enough impact to significantly alter the fit. However, we have not proceeded with a detailed fit of this component, as there are many parameters and the solution would be degenerate (e.g. grain size distribution, gas density, ISRF intensity, as well as radiative transfer considerations). We have kept the analysis simple, which allows us to say that we have definitely detected anomalous microwave emission, that it is associated with the molecular

phase, and that spinning dust provides a good model with which to understand the spectrum of this excess emission. Some of this emission could be explained by free-free emission, but it cannot be the dominant emission mechanism in this phase.

To study the possibility that spinning dust emission is present in either the atomic or ionised phase, we have also estimated its contribution to these. The different environments will have an impact on the spinning dust emission, so we have adapted the gas parameters in the modelling. For the atomic phase we have used the results of Heiles & Troland (2003) and modelled the atomic ISM as composed of 40% cold neutral medium (CNM) and 60% warm neutral medium (WNM). The parameters for these phases are $n_H = 30$ cm⁻³ and $T_{\text{gas}} = 100$ K for the CNM, and $n_H = 0.4$ cm⁻³ and $T_{\text{gas}} = 6000$ K for the WNM. As can be seen in Fig. 6, the SEDs show that spinning dust emission is able to reproduce the departure from the thermal dust spectrum for $\nu < 70$ GHz. The 1.4 GHz point in the last atomic template is almost certainly an artifact. The atomic and synchrotron templates both describe diffuse smooth emission in the Galaxy, leading to some “crosstalk” between the two components. However it should be noted that when the emissivity found for the atomic phase in the outer Galaxy is multiplied by the column density of hydrogen in the template, the total emission is very low, lower than the noise level derived for the 1.4 GHz map. As such, it should not be viewed as significant.

For the ionised phase, we use the same gas parameters as in Sect. 2.2, namely $n_H = 10$ cm⁻³ and $T_{\text{gas}} = 8000$ K. The SED in Fig. 8 shows that spinning dust may also be present in this phase, but that it is completely dominated by free-free emission. In fact, the situation may be even worse, as we have assumed solar value PAH abundance, whereas recently Dobler et al. (2009) showed that the PAH abundance in this type of region is about a factor of three lower.

Assuming that the atomic, molecular and dark gas contributions at 30 GHz are due solely to spinning dust, and that the ionised phase has a negligible contribution, we have produced a Galactic-plane image of spinning dust emission. This provides a complementary image to that presented in Planck Collaboration (2011d), as it has been obtained using a different approach. The intensity map is shown at the top of Fig. 12; at the bottom we show the fraction of the total signal at 30 GHz due to spinning dust. Several bright regions show up in this map, highlighting areas where spinning dust emission is the dominant source of

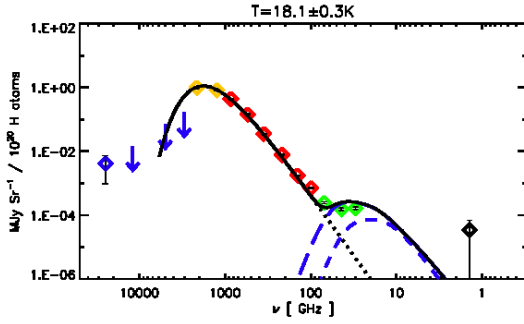


Fig. 13. The resulting SED for the dark gas component. The different lines and colours are as described in Fig. 6. The dashed and short-dashed lines shows the spinning dust contribution from a molecular phase, and from an atomic phase, respectively.

emission at these frequencies. Overall, spinning dust accounts for $25 \pm 5\%$ (statistical) of the total emission at 30 GHz. This error estimate does not take into account any systematic uncertainty due to our simple model, which is difficult to quantify, and so will likely be higher.

4.3. Dark gas

Dark gas has been detected in numerous studies (Reach et al. 1994; Grenier et al. 2005) as an infrared, and a correlated infrared/gamma-ray, excess over and above what is expected given the gas column density derived from H I and CO data. The inversion performed without this component results in positive and negative residuals, as the other components compete to account for this missing gas phase. Not only does adding this component lower our reduced χ^2 fits *across all bands*, but it also allows us to examine the nature of this dark component.

Looking at Fig13, the resulting SED for this component looks quite similar to both the atomic and molecular SEDs. Its temperature does not differentiate it immediately from either of the two phases, and it shows a low-frequency tail beyond the thermal dust SED. These points look similar to the anomalous dust in the molecular phase (dashed line); however, the spinning dust model lies above the LFI points. Assuming that the spinning dust is in an atomic phase (dotted line), it can be seen that it does not predict the observed emission. It thus seems to be more of a mix of the two phases, with a larger influence from the molecular phase. The different parameters discussed in Sect. 4.2.3 could also be altered, but we do not have enough data to constrain such a fit.

The interpretation of these results is somewhat complicated for several reasons. Firstly, the amount of dark gas is not expected to be independent of Galactic position, but using a 2D template we are forced to assume just that. Secondly, the estimate of this gas phase was obtained at high galactic latitude and we are using an extrapolation into the Galactic plane. It would be preferable to use an independent template, derived from gamma-ray observations for example, in future inversion analyses. Reconstructing the line-of-sight distribution of the dark gas would enable a more exact determination of the properties of the dark gas, by coupling the analysis with a 3D extinction map (e.g. Drimmel et al. 2003; Marshall et al. 2006; Sale et al. 2009). This type of analysis will be considered in a future study of the Galactic inversion.

In summary, the dark gas SED is consistent with molecular gas, most likely diffuse H₂ and optically thick CO. The best fit

at longer wavelengths comes from the spinning dust model, in a molecular medium.

5. Possible sources of bias

Our inversion algorithm determines the flux density per column density of each template, and hence the result depends on the different templates themselves. Care should therefore be taken to use the most physically representative input for each phase of the ISM that we want to include in the inversion. Nonetheless, the jackknife tests described in Sect. 3.3 show that the method is self-consistent. Moreover, many different combinations for the H I+CO Galactocentric rings has been attempted, and the main results presented here remain coherent with those. However, the results are notably sensitive to one particular input, the synchrotron template. Without it, the H I templates trace the Galactic synchrotron emission, as the H I observations trace the large-scale smooth structure of the Milky Way, similar to the diffuse soft synchrotron emission. This artificial component in the H I templates then masks any contribution for the anomalous microwave emission. We have attempted to trace the synchrotron emission with two different synchrotron templates: the WMAP MCMC synchrotron template (Gold et al. 2009); and the 408 MHz full sky survey (Haslam et al. 1982). We have decided to use the latter as it more successfully removes the synchrotron contribution from the H I templates and allows us to detect anomalous emission in the atomic phase.

5.1. Correlation between parameters and uniqueness of the solution

In Fig. 14 we show the correlation between the different emissivities of our best solution at 30 GHz, where many emission mechanisms are present and the inversion is more challenging. These were obtained from the result of the jackknife tests presented in Sect. 3.3. It can be seen that for almost all the templates the correlation is low. Three elements are to be highlighted. The first one is that the emissivities for the outer Galaxy molecular template, as well as the ionised template, both have pronounced departures from a Gaussian distribution. Looking at Fig. 1, both templates are patchy; the masking of several regions simultaneously will change the morphology of each map significantly and therefore have a large impact on the derived emissivity.

Secondly, rings 1–3 of the atomic and molecular phase are slightly anti-correlated (the contours are elliptical). This region of the Galaxy is indeed difficult to disentangle, and due to the low filling factor of these rings the algorithm has less to work with than in the solar circle, for example. Nevertheless the error bars deduced from the jackknife analysis account for this slight degeneracy. Higher resolution maps will help reduce this crosstalk between templates in future analyses.

Thirdly a small bias can be seen, as the results of the inversion are not always centred in the middle of the jackknife distributions. We calculated this bias by looking at the difference between the mean deviation of each result with respect to the jackknife realisations, in units of result uncertainty. That is the bias B per template i and per band ν can be written:

$$B(i, \nu) = \frac{1}{\sigma(i, \nu)} \frac{1}{N_r} \sum_{r=1}^{N_r} [\epsilon(i, \nu) - \epsilon_j(r, i, \nu)], \quad (10)$$

where N_r is the number of jackknife realisations, $\epsilon(i, \nu)$ and $\sigma(i, \nu)$ are the result and uncertainty of the inversion, and $-\epsilon_j(r, i, \nu)$ is the result of one jackknife realisation. We have

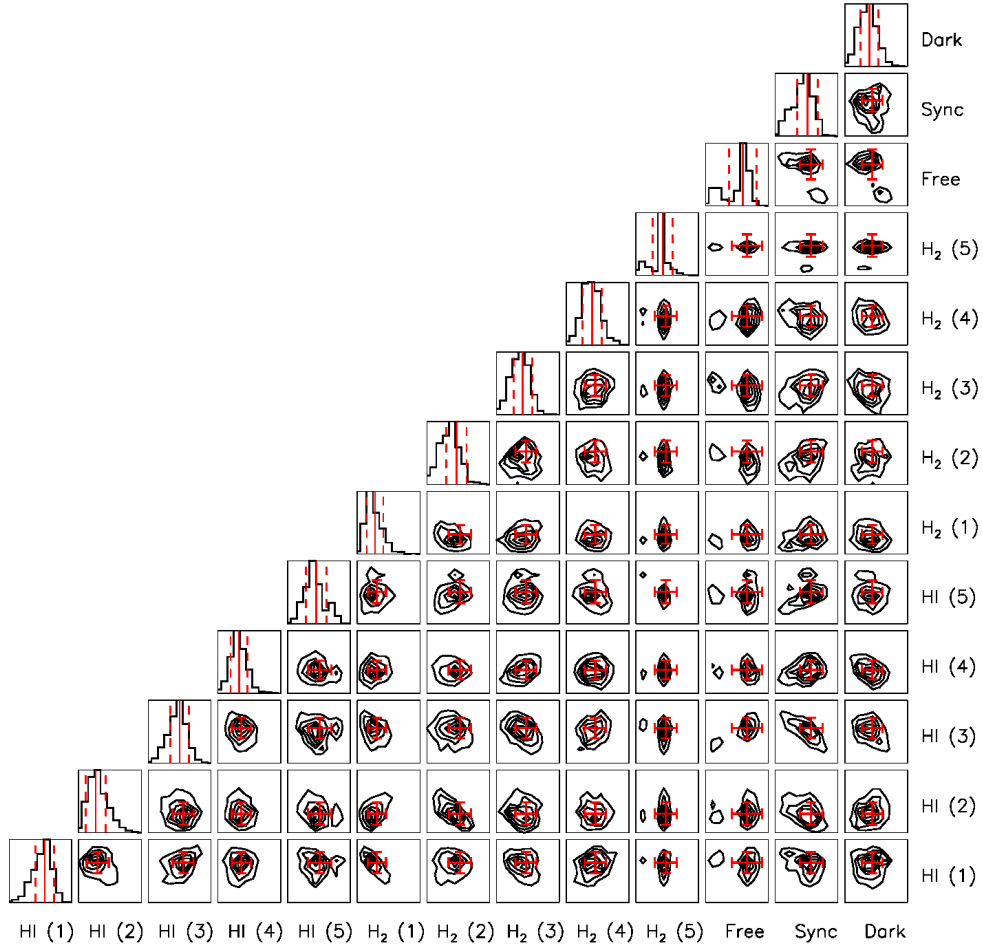


Fig. 14. Correlation matrix of the emissivities for each ring at 30 GHz. Overplotted in red are the results with corresponding error bars. One-dimensional histograms replace the contour plots where only one component is concerned.

found this effect to be small, with a median bias of 0.005σ over all templates and frequencies, and with a mean absolute deviation of 0.08σ . In all cases, the bias is always lower than 0.25σ .

5.2. Effect of CMB subtraction

The CMB removal in the *Planck* maps we have used may create significant residuals in the Galactic plane. Therefore, to test the impact of the CMB removal on our results, a different CMB estimate was reconstructed through a classical Internal Linear Combination (ILC) by means of Lagrange multipliers (Eriksen et al. 2004). A $\pm 15^\circ$ strip in Galactic latitude was extracted from the HFI CMB frequency channels maps (100, 143, 217 and 353 GHz) reduced to a common resolution (10 arcmin), in units of K_{CMB} . This CMB component was subtracted from all the *Planck* LFI and HFI channels maps, resulting in a new and independent set of CMB-removed *Planck* maps.

Even though the methods are similar, the resulting CMB in the Galactic plane is quite different. In constructing the standard CMB subtraction (Needlet ILC, “NILC”), an intensity mask was applied (Planck HFI Core Team 2011) which results in CMB residuals remaining in a substantial part of the Galactic plane. No such mask was used in the Galactic plane ILC. Outside of this mask, the differences between the two CMB estimates are

of the same order as the residuals of our fit at low frequencies, $44 \text{ GHz} < \nu < 143 \text{ GHz}$.

Using these maps to perform the same inversion, we have concluded that the impact is small, and almost always within the error bars. In Fig. 15 we plot the derived emissivities using the NILC and the Galactic plane centred CMB removal (“ILC”).

To get a better idea of where the solution might be off by more than 1σ , we show the difference in units of σ per band in Fig. 16. The value plotted is, for each component:

$$\Delta_\sigma = \frac{\epsilon_{\text{ILC}} - \epsilon_{\text{NILC}}}{\sqrt{(\delta\epsilon_{\text{ILC}}^2 + \delta\epsilon_{\text{NILC}}^2)}}. \quad (11)$$

The agreement is generally very good, except for some points concentrated in the bands 143, 100 and 70 GHz. In these cases the CO templates are higher in the Galactic plane ILC whereas the H I and H^+ templates are lower. Nevertheless, there are no points that are different by more than 3σ . Therefore, these differences do not change our main conclusions, but would slightly modify the amount of anomalous emission, for example. As we are not modelling the specifics of any emission mechanisms at the lower frequencies, we are not sensitive to the impact of the CMB removal for this study.

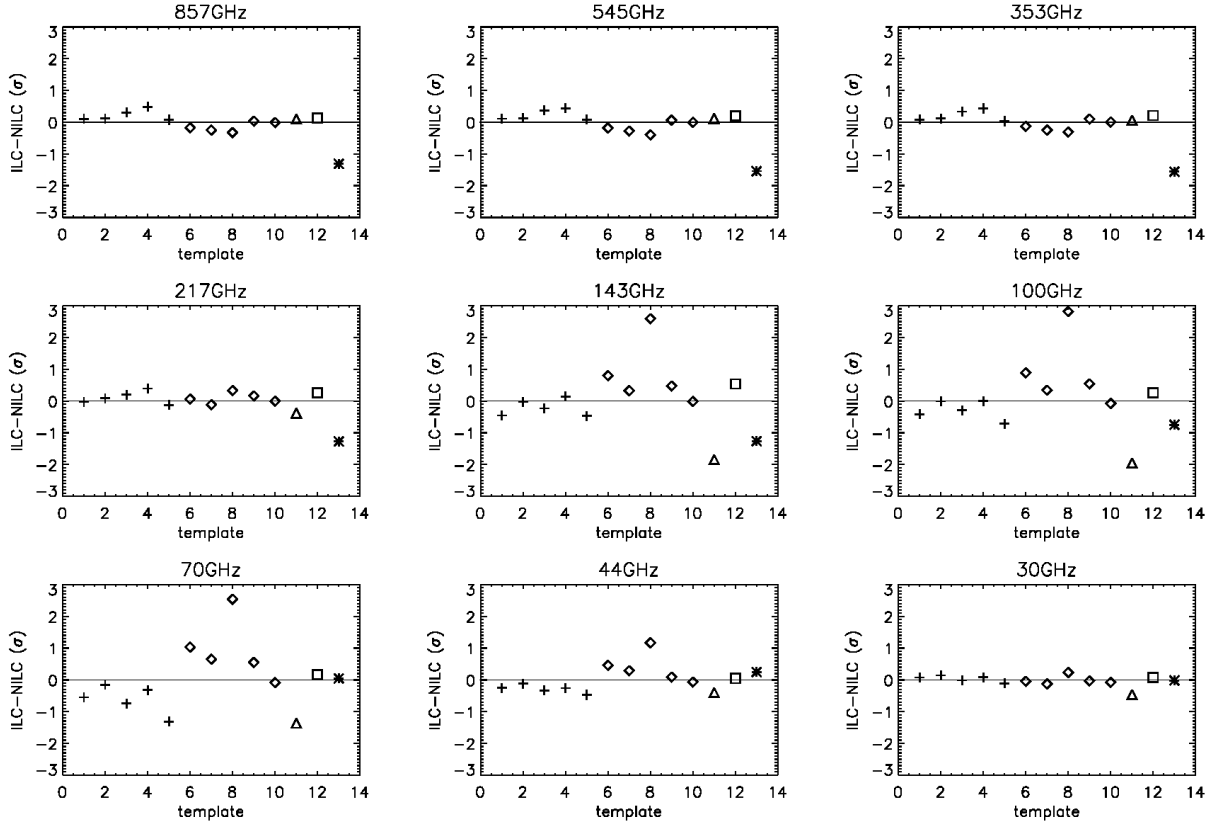


Fig. 16. Comparison of emissivities derived after application of two different CMB subtractions. The value plotted is shown in Eq. 11. The symbols represent H I (plus), H₂ (diamond), H⁺ (triangle), Synchrotron (square) and dark gas (asterisk). Differences are generally small, but become larger in the range 143–44 GHz.

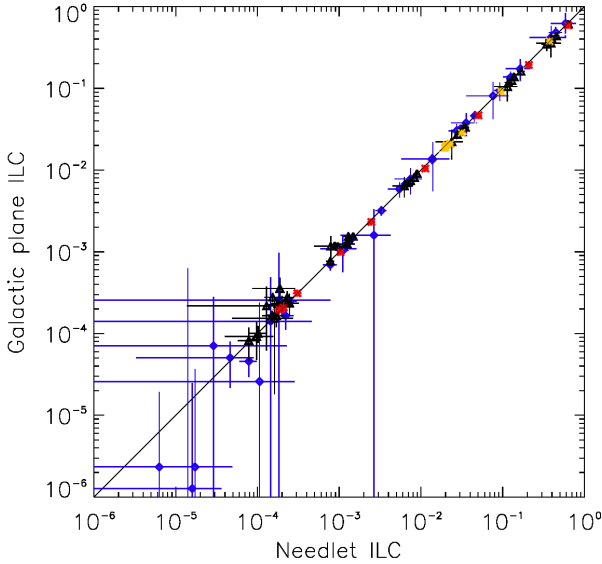


Fig. 15. Comparison of emissivities derived after application of two different CMB subtractions, the official Needlet ILC and the Galactic plane ILC. The atomic templates are the blue points, molecular are black, ionised is orange, dark gas is red and synchrotron is green.

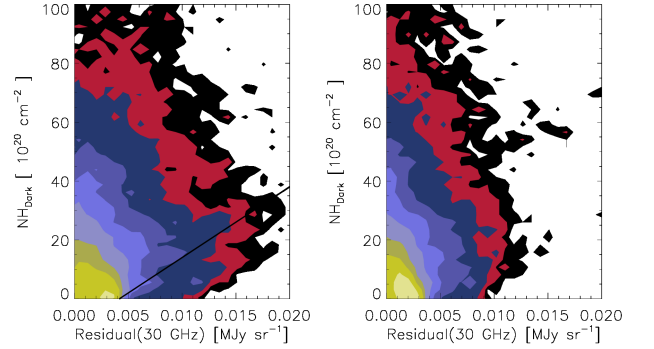


Fig. 17. Dark gas intensity as a function of the residuals of the inversion at 30 GHz without (Left) and with (Right) the dark gas template. A distinct component of the residual (shown with the solid line) is seen to be correlated with the dark gas template. This correlated residual disappears when the dark gas is used in the inversion.

5.3. Impact of using dark gas template

The dark gas template used in this study has been calculated by Planck Collaboration (2011c). It is the result of finding at what column densities the correlation between total hydrogen column density (H I + 2H₂) versus optical depth of the dust departs from linearity. The frequencies used to obtain the map at 857 GHz that we use as a template are 857 and 545 GHz, along with the *IRAS* 100 μ m band. There is some circularity in using a template based on a residual in the *Planck* data to fit the same data. However, the

data used is restricted to the two highest HFI frequencies. Here we present the impact at 30 GHz, which in no respect suffers from the same circularity, as the data are far from the frequencies used to derive the dark gas template, and they come from LFI, a completely separate instrument from HFI.

We have performed the inversion with and without the dark gas template at 30 GHz, and looked at the correlation between the residuals and the column density of the dark gas. The results are shown in Fig. 17; the inversion performed without the dark gas template is on the left, the same inversion with the dark gas template is on the right. A distinct component of the residuals can be seen to correlate very well with the dark gas column density when the dark gas template is not used. This correlation completely disappears when it is used. In addition, the reduced χ^2 for the fit shows a significant improvement of approximately 50%.

The choice of both the opacity correction for the H I and the X_{CO} value chosen will have an impact on our results. We have chosen to keep the analysis simple for this study, as the spin temperature we assume, together with the dark gas template, should account for most of the optically thick gas in the plane. The ability of the dark gas template used to adequately account for all the optically thick gas remains to be studied, so future work could involve using more sophisticated methods to account for this effect.

6. Conclusions

The analysis performed in this study provides a realistic description of the dust and gas properties as a function of Galactic radius in the Milky Way. The dust temperature in the H I is seen to decrease as a function of Galactocentric distance from 24.0 to 13.9 K, and the temperature in the molecular phase is heated by star formation associated to the Galactic spiral arms. The opacity found for grains in the solar circle is $\tau/N_{\text{H}} = 0.92 \pm 0.05 \times 10^{-25} \text{ cm}^2$, and with no significant variation with Galactic radius, even though the dust temperature is seen to drop by over 10 K from the centre to the outer Galaxy. The dust temperature in the H I gas in the solar circle, $17.6 \pm 0.1 \text{ K}$ is also compatible with the recent *Planck* value of high-latitude cirrus ($17.8 \pm 0.9 \text{ K}$).

The extension of our analysis to lower frequencies than previously used in inversion techniques has allowed us to place constraints on the free-free, synchrotron and anomalous microwave emission:

- Anomalous dust emission is clearly seen in the atomic, molecular and dark gas phases. It is well fit by a very simple model consisting of spinning PAH molecules embedded in each of the gas phases. We highlight regions where spinning dust emission may be strong with respect to other emission mechanisms. According to our simple model, in the Galactic plane spinning dust accounts for $25 \pm 5\%$ (statistical) of the total emission at 30 GHz. However, systematic uncertainties linked to our model may make this value more uncertain.
- The dark gas phase has been explored spectrally across the Galactic plane for the first time. Its SED is similar to the molecular phase and therefore this phase seems to be tracing diffuse H_2 where CO is disassociated by energetic photons, as well as tracing optically thick CO and H I.
- The free-free emission is completely traced by our ionised component and indicates that the free-free estimate from *WMAP* component separation methods may be too high. In the ionised phase, spinning dust may be present but it is dominated by free-free emission.

- Synchrotron emission is well characterised by a power law with a spectral index of -1.0 .

This first analysis of the large-scale Galactic emission as seen by *Planck* has constrained the large scale ISM properties in the Galaxy. It could be improved in the future via several modifications. Individual regions could be studied using higher angular resolution data, which would probe smaller scale fluctuations that have been missed by the present study. The radial separation could be done differently to explore the difference between arm and inter-arm ISM, in order to focus more on the role of ISM conditions on the star formation process. It should also be possible to obtain an independent estimate of the dark gas in the plane, and ideally some radial information about its behaviour. In the near future, *Planck* component separation products could be used in the place of *WMAP* ones. Use of radio recombination line surveys currently underway would be very useful to constrain the free-free emission in the plane, and as a function of Galactic radius.

Acknowledgements. A description of the Planck Collaboration and a list of its members can be found at http://www.rssd.esa.int/index.php?project=PLANCK&page=Planck_Collaboration

References

- Abdo, A. A., Ackermann, M., Ajello, M., et al. 2010, *ApJ*, 710, 133
Ackermann, M., Ajello, M., Baldini, L., et al. 2011, *ApJ*, 726, 81
Ali-Haïmoud, Y., Hirata, C. M., & Dickinson, C. 2009, *MNRAS*, 395, 1055
Alves, M. I. R., Davies, R. D., Dickinson, C., et al. 2010, *MNRAS*, 405, 1654
Banday, A. J., Dickinson, C., Davies, R. D., Davis, R. J., & Górski, K. M. 2003, *MNRAS*, 345, 897
Bennett, C. L., Hill, R. S., Hinshaw, G., et al. 2003, *ApJS*, 148, 97
Binney, J. & Merrifield, M. 1998, *Galactic astronomy* / James Binney and Michael Merrifield. Princeton
Bloemen, J. B. G. M., Deul, E. R., & Thaddeus, P. 1990, *A&A*, 233, 437
Bloemen, J. B. G. M., Strong, A. W., Mayer-Hasselwander, H. A., et al. 1986, *A&A*, 154, 25
Boughn, S. P. & Pober, J. C. 2007, *ApJ*, 661, 938
Casassus, S., Cabrera, G. F., Förster, F., et al. 2006, *ApJ*, 639, 951
Casassus, S., Nyman, L.-Å., Dickinson, C., & Pearson, T. J. 2007, *MNRAS*, 382, 1607
Clemens, D. P. 1985, Ph.D. Thesis Massachusetts Univ., 3
Compiègne, M., Verstraete, L., Jones, A., et al. 2011, *A&A*, 525, A103+
Dame, T. M., Hartmann, D., & Thaddeus, P. 2001, *ApJ*, 547, 792
Davies, R. D., Dickinson, C., Banday, A. J., et al. 2006, *MNRAS*, 370, 1125
Dickey, J. M., McClure-Griffiths, N. M., Gaensler, B. M., & Green, A. J. 2003, *ApJ*, 585, 801
Dickey, J. M., Strasser, S., Gaensler, B. M., et al. 2009, *ApJ*, 693, 1250
Dickinson, C., Casassus, S., Davies, R. D., et al. 2010, *MNRAS*, 407, 2223
Dickinson, C., Davies, R. D., Bronfman, L., et al. 2007, *MNRAS*, 379, 297
Dobler, G., Draine, B., & Finkbeiner, D. P. 2009, *ApJ*, 699, 1374
Draine, B. T. & Lazarian, A. 1998, *ApJ Letters* v.494, 494, L19
Drimmel, R., Cabrera-Lavers, A., & López-Corredoira, M. 2003, *A&A*, 409, 205
Dunkley, J., Komatsu, E., Nolte, M. R., et al. 2009, *ApJS*, 180, 306
Eriksen, H. K., Banday, A. J., Górski, K. M., & Lilje, P. B. 2004, *ApJ*, 612, 633
Finkbeiner, D. P. 2004, *ApJ*, 614, 186
Giard, M., Lamarre, J. M., Pajot, F., & Serra, G. 1994, *A&A*, 286, 203
Gold, B., Bennett, C. L., Hill, R. S., et al. 2009, *ApJS*, 180, 265
Górski, K. M., Hivon, E., Banday, A. J., et al. 2005, *ApJ*, 622, 759
Grenier, I. A., Casandjian, J.-M., & Terrier, R. 2005, *Science*, 307, 1292
Haslam, C. G. T., Salter, C. J., Stoffel, H., & Wilson, W. E. 1982, *A&AS*, 47, 1
Hauser, M. G., Arendt, R. G., Kelsall, T., et al. 1998, *ApJ*, 508, 25
Heiles, C. & Troland, T. H. 2003, *ApJ*, 586, 1067
Jarosik, N., Bennett, C. L., Dunkley, J., et al. 2011, *ApJS*, 192, 14
Kalberla, P. M. W., Burton, W. B., Hartmann, D., et al. 2005, *A&A*, 440, 775
Kogut, A., Banday, A. J., Bennett, C. L., et al. 1996, *ApJ*, 460, 1
Leach, S. M., Cardoso, J., Baccigalupi, C., et al. 2008, *A&A*, 491, 597
Marshall, D. J., Robin, A. C., Reylé, C., Schultheis, M., & Picaud, S. 2006, *A&A*, 453, 635
Mathis, J. S., Mezger, P. G., & Panagia, N. 1983, *A&A*, 128, 212
Miville-Deschênes, M.-A. & Lagache, G. 2005, *ApJS*, 157, 302
Miville-Deschênes, M.-A., Ysard, N., Lavabre, A., et al. 2008, *A&A*, 490, 1093

- Neugebauer, G., Habing, H. J., van Duinen, R., et al. 1984, *ApJ*, 278, L1
- Paladini, R., Montier, L., Giard, M., et al. 2007, *A&A*, 465, 839
- Planck Collaboration. 2011a, Planck early results 16: The Planck view of nearby galaxies (Submitted to *A&A*, [arXiv:astro-ph/1101.2045])
- Planck Collaboration. 2011b, Planck early results 17: Origin of the submillimetre excess dust emission in the Magellanic Clouds (Submitted to *A&A*, [arXiv:astro-ph/1101.2046])
- Planck Collaboration. 2011c, Planck early results 19: All-sky temperature and dust optical depth from Planck and IRAS — constraints on the “dark gas” in our Galaxy (Submitted to *A&A*, [arXiv:astro-ph/1101.2029])
- Planck Collaboration. 2011d, Planck early results 20: New light on anomalous microwave emission from spinning dust grains (Submitted to *A&A*, [arXiv:astro-ph/1101.2031])
- Planck Collaboration. 2011e, Planck early results 22: The submillimetre properties of a sample of Galactic cold clumps (Submitted to *A&A*, [arXiv:astro-ph/1101.2034])
- Planck Collaboration. 2011f, Planck early results 23: The Galactic cold core population revealed by the first all-sky survey (Submitted to *A&A*, [arXiv:astro-ph/1101.2035])
- Planck Collaboration. 2011g, Planck early results 24: Dust in the diffuse interstellar medium and the Galactic halo (Submitted to *A&A*, [arXiv:astro-ph/1101.2036])
- Planck Collaboration. 2011h, Planck early results 25: Thermal dust in nearby molecular clouds (Submitted to *A&A*, [arXiv:astro-ph/1101.2037])
- Planck HFI Core Team. 2011, Planck early results 06: The High Frequency Instrument data processing (Submitted to *A&A*, [arXiv:astro-ph/1101.2048])
- Porter, T. A., Moskalenko, I. V., Strong, A. W., Orlando, E., & Bouchet, L. 2008, *ApJ*, 682, 400
- Press, W. H., Teukolsky, S. A., Vetterling, W. T., & Flannery, B. P. 1992, *Numerical recipes in FORTRAN. The art of scientific computing*, ed. Press, W. H., Teukolsky, S. A., Vetterling, W. T., & Flannery, B. P.
- Reach, W. T., Koo, B.-C., & Heiles, C. 1994, *ApJ*, 429, 672
- Reich, P. & Reich, W. 1986, *A&AS*, 63, 205
- Reich, P., Testori, J. C., & Reich, W. 2001, *A&A*, 376, 861
- Reich, W. 1982, *A&AS*, 48, 219
- Rouan, D., Leger, A., Omont, A., & Giard, M. 1992, *A&A*, 253, 498
- Sale, S. E., Drew, J. E., Unruh, Y. C., et al. 2009, *MNRAS*, 392, 497
- Scaife, A. M. M., Hurley-Walker, N., Davies, M. L., et al. 2008, *MNRAS*, 385, 809
- Scaife, A. M. M., Hurley-Walker, N., Green, D. A., et al. 2009, *MNRAS*, 400, 1394
- Scaife, A. M. M., Nikolic, B., Green, D. A., et al. 2010, *MNRAS: Letters*, 406, L45
- Silsbee, K., Ali-Haïmoud, Y., & Hirata, C. M. 2011, *MNRAS*, 411, 2750
- Sodroski, T. J., Dwek, E., Hauser, M. G., & Kerr, F. J. 1989, *ApJ*, 336, 762
- Sodroski, T. J., Odegard, N., Arendt, R. G., et al. 1997, *ApJ*, 480, 173
- Tielens, A. G. G. M. 2005, *The Physics and Chemistry of the Interstellar Medium*, ed. Tielens, A. G. G. M.
- Watson, R. A., Rebolo, R., Rubiño-Martín, J. A., et al. 2005, *ApJ*, 624, L89
- Weingartner, J. C. & Draine, B. T. 2001, *ApJ*, 548, 296
- Ysard, N., Miville-Deschênes, M. A., & Verstraete, L. 2010, *A&A*, 509, L1
- Ysard, N. & Verstraete, L. 2010, *A&A*, 509, 12
- Zacchei, A., Maino, D., Baccigalupi, C. et al. 2011, Planck early results 05: The Low Frequency Instrument data processing (Submitted to *A&A*, [arXiv:astro-ph/1101.2040])

Appendix A: Table of results

Table A.1. Result of the inversion per band and per component in MJy sr⁻¹ / 10²⁰ H atoms, except for the synchrotron component in which case it is in MJy sr⁻¹(ν) per MJy sr⁻¹(408 MHz).

Band [GHz]	H I(1)	H I(2)	H I(3)	H I(4)	H I(5)
25000	$1.4 \pm 0.4 \times 10^{-1}$	$5 \pm 3 \times 10^{-2}$	$7.8 \pm 0.6 \times 10^{-2}$	$2.4 \pm 0.2 \times 10^{-2}$	$6.0 \pm 0.9 \times 10^{-3}$
12000	$<1.5 \times 10^{-1}$	$<4.6 \times 10^{-2}$	$8.2 \pm 1.3 \times 10^{-2}$	$<1.2 \times 10^{-2}$	$<5.9 \times 10^{-3}$
5000	$8 \pm 3 \times 10^{-1}$	$3 \pm 2 \times 10^{-1}$	$4.1 \pm 0.5 \times 10^{-1}$	$<6.2 \times 10^{-2}$	$<2.5 \times 10^{-2}$
3000	3.3 ± 1.5	2 ± 1	1.8 ± 0.2	$5.9 \pm 0.6 \times 10^{-1}$	$<4.6 \times 10^{-2}$
2143	4.9 ± 1.2	3.0 ± 0.8	2.6 ± 0.2	1.3 ± 0.1	$2.6 \pm 0.3 \times 10^{-1}$
1250	1.5 ± 0.6	1.6 ± 0.4	1.5 ± 0.1	$9.7 \pm 0.4 \times 10^{-1}$	$4.0 \pm 0.1 \times 10^{-1}$
857	$8 \pm 2 \times 10^{-1}$	$9.2 \pm 1.7 \times 10^{-1}$	$7.7 \pm 0.3 \times 10^{-1}$	$5.7 \pm 0.1 \times 10^{-1}$	$3.2 \pm 0.1 \times 10^{-1}$
545	$1.9 \pm 0.7 \times 10^{-1}$	$2.9 \pm 0.5 \times 10^{-1}$	$2.3 \pm 0.1 \times 10^{-1}$	$2.0 \pm 0.1 \times 10^{-1}$	$1.4 \pm 0.1 \times 10^{-1}$
353	$3.8 \pm 1.5 \times 10^{-2}$	$6.7 \pm 1.2 \times 10^{-2}$	$5.4 \pm 0.2 \times 10^{-2}$	$4.9 \pm 0.1 \times 10^{-2}$	$4.0 \pm 0.1 \times 10^{-2}$
217	$6 \pm 3 \times 10^{-3}$	$1.4 \pm 0.3 \times 10^{-2}$	$1.1 \pm 0.1 \times 10^{-2}$	$1.1 \pm 0.1 \times 10^{-2}$	$9.5 \pm 0.1 \times 10^{-3}$
143	$1.1 \pm 0.7 \times 10^{-3}$	$2.7 \pm 0.5 \times 10^{-3}$	$2.4 \pm 0.1 \times 10^{-3}$	$2.3 \pm 0.1 \times 10^{-3}$	$2.3 \pm 0.1 \times 10^{-3}$
100	$<7.3 \times 10^{-4}$	$6 \pm 2 \times 10^{-4}$	$5.8 \pm 0.6 \times 10^{-4}$	$5.9 \pm 0.3 \times 10^{-4}$	$7.6 \pm 0.1 \times 10^{-4}$
70	$<4.1 \times 10^{-4}$	$1.1 \pm 0.9 \times 10^{-4}$	$1.6 \pm 0.5 \times 10^{-4}$	$1.3 \pm 0.1 \times 10^{-4}$	$2.9 \pm 0.1 \times 10^{-4}$
44	$<3.3 \times 10^{-4}$	$<8.9 \times 10^{-5}$	$9 \pm 4 \times 10^{-5}$	$8.3 \pm 1.3 \times 10^{-5}$	$1.4 \pm 0.2 \times 10^{-4}$
30	$<3.4 \times 10^{-4}$	$1.5 \pm 1.2 \times 10^{-4}$	$1.3 \pm 0.4 \times 10^{-4}$	$1.4 \pm 0.1 \times 10^{-4}$	$1.2 \pm 0.2 \times 10^{-4}$
1.4	$<1.1 \times 10^{-3}$	$<3.8 \times 10^{-4}$	$<3.1 \times 10^{-4}$	$<1.7 \times 10^{-4}$	$4 \pm 2 \times 10^{-4}$
Band [GHz]	H ₂ (1)	H ₂ (2)	H ₂ (3)	H ₂ (4)	H ₂ (5)
25000	$2.3 \pm 1.3 \times 10^{-2}$	$6.2 \pm 0.6 \times 10^{-2}$	$9 \pm 6 \times 10^{-3}$	$8 \pm 4 \times 10^{-3}$	$3.0 \pm 0.6 \times 10^{-2}$
12000	$4.8 \pm 1.9 \times 10^{-2}$	$5.1 \pm 1.0 \times 10^{-2}$	$4.8 \pm 1.1 \times 10^{-2}$	$<1.8 \times 10^{-2}$	$<3.6 \times 10^{-2}$
5000	$1.7 \pm 1.3 \times 10^{-1}$	$5.7 \pm 0.7 \times 10^{-1}$	$2.5 \pm 0.7 \times 10^{-1}$	$<8.1 \times 10^{-2}$	$<1.8 \times 10^{-1}$
3000	1.4 ± 0.6	2.3 ± 0.3	$8 \pm 2 \times 10^{-1}$	$2.7 \pm 1.0 \times 10^{-1}$	$9 \pm 2 \times 10^{-1}$
2143	2.8 ± 0.4	3.6 ± 0.2	1.8 ± 0.2	$4.3 \pm 0.9 \times 10^{-1}$	$1.5 \pm 0.3 \times 10^0$
1250	2.0 ± 0.2	2.1 ± 0.1	1.3 ± 0.1	$5.3 \pm 0.4 \times 10^{-1}$	$1.1 \pm 0.1 \times 10^0$
857	$8.0 \pm 0.8 \times 10^{-1}$	$8.3 \pm 0.4 \times 10^{-1}$	$6.1 \pm 0.4 \times 10^{-1}$	$3.8 \pm 0.2 \times 10^{-1}$	$6.1 \pm 0.5 \times 10^{-1}$
545	$2.1 \pm 0.2 \times 10^{-1}$	$2.1 \pm 0.1 \times 10^{-1}$	$1.7 \pm 0.1 \times 10^{-1}$	$1.4 \pm 0.1 \times 10^{-1}$	$2.1 \pm 0.1 \times 10^{-1}$
353	$4.3 \pm 0.5 \times 10^{-2}$	$4.1 \pm 0.3 \times 10^{-2}$	$3.7 \pm 0.2 \times 10^{-2}$	$3.7 \pm 0.1 \times 10^{-2}$	$5.3 \pm 0.3 \times 10^{-2}$
217	$1.1 \pm 0.1 \times 10^{-2}$	$1.0 \pm 0.1 \times 10^{-2}$	$9.5 \pm 0.4 \times 10^{-3}$	$1.0 \pm 0.1 \times 10^{-2}$	$1.4 \pm 0.1 \times 10^{-2}$
143	$1.4 \pm 0.2 \times 10^{-3}$	$1.3 \pm 0.1 \times 10^{-3}$	$1.2 \pm 0.1 \times 10^{-3}$	$1.7 \pm 0.1 \times 10^{-3}$	$2.3 \pm 0.2 \times 10^{-3}$
100	$1.9 \pm 0.1 \times 10^{-3}$	$1.6 \pm 0.1 \times 10^{-3}$	$1.5 \pm 0.1 \times 10^{-3}$	$1.6 \pm 0.1 \times 10^{-3}$	$1.7 \pm 0.2 \times 10^{-3}$
70	$2.1 \pm 0.5 \times 10^{-4}$	$1.8 \pm 0.2 \times 10^{-4}$	$2.2 \pm 0.3 \times 10^{-4}$	$2.3 \pm 0.1 \times 10^{-4}$	$3.7 \pm 1.6 \times 10^{-4}$
44	$1.9 \pm 0.4 \times 10^{-4}$	$1.7 \pm 0.3 \times 10^{-4}$	$2.4 \pm 0.3 \times 10^{-4}$	$1.3 \pm 0.1 \times 10^{-4}$	$4.4 \pm 1.9 \times 10^{-4}$
30	$2.8 \pm 0.4 \times 10^{-4}$	$2.5 \pm 0.4 \times 10^{-4}$	$3.1 \pm 0.3 \times 10^{-4}$	$1.3 \pm 0.1 \times 10^{-4}$	$6 \pm 2 \times 10^{-4}$
1.4	$<3.6 \times 10^{-4}$	$<1.6 \times 10^{-4}$	$<1.7 \times 10^{-4}$	$<8.5 \times 10^{-5}$	$<5.9 \times 10^{-3}$
Band [GHz]	H II	Sync.	Dark		
25000	$9.7 \pm 0.9 \times 10^{-1}$	—	$4 \pm 3 \times 10^{-3}$		
12000	3.3 ± 0.3	—	$<1.5 \times 10^{-2}$		
5000	$1.9 \pm 0.1 \times 10^1$	—	$<7.1 \times 10^{-2}$		
3000	$2.8 \pm 0.1 \times 10^1$	—	$<1.7 \times 10^{-1}$		
2143	$2.9 \pm 0.1 \times 10^1$	—	1.0 ± 0.1		
1250	$1.2 \pm 0.1 \times 10^1$	—	$8.3 \pm 0.4 \times 10^{-1}$		
857	4.7 ± 0.2	—	$4.4 \pm 0.2 \times 10^{-1}$		
545	1.3 ± 0.1	—	$1.5 \pm 0.1 \times 10^{-1}$		
353	$3.1 \pm 0.1 \times 10^{-1}$	—	$3.5 \pm 0.1 \times 10^{-2}$		
217	$7.9 \pm 0.2 \times 10^{-2}$	—	$7.9 \pm 0.2 \times 10^{-3}$		
143	$3.0 \pm 0.1 \times 10^{-2}$	—	$1.8 \pm 0.1 \times 10^{-3}$		
100	$2.3 \pm 0.1 \times 10^{-2}$	$3 \pm 2 \times 10^{-3}$	$7.1 \pm 0.3 \times 10^{-4}$		
70	$2.2 \pm 0.1 \times 10^{-2}$	$<4.7 \times 10^{-3}$	$2.5 \pm 0.2 \times 10^{-4}$		
44	$2.3 \pm 0.1 \times 10^{-2}$	$9 \pm 3 \times 10^{-3}$	$1.5 \pm 0.2 \times 10^{-4}$		
30	$2.2 \pm 0.1 \times 10^{-2}$	$2.0 \pm 0.3 \times 10^{-2}$	$1.7 \pm 0.2 \times 10^{-4}$		
1.4	$1.8 \pm 0.1 \times 10^{-2}$	$2.9 \pm 0.1 \times 10^{-1}$	$<3.5 \times 10^{-5}$		

-
- ¹ Aalto University Metsähovi Radio Observatory, Metsähovintie 114, FIN-02540 Kylmälä, Finland
- ² Agenzia Spaziale Italiana Science Data Center, c/o ESRIN, via Galileo Galilei, Frascati, Italy
- ³ Astroparticule et Cosmologie, CNRS (UMR7164), Université Denis Diderot Paris 7, Bâtiment Condorcet, 10 rue A. Domon et Léonie Duquet, Paris, France
- ⁴ Astrophysics Group, Cavendish Laboratory, University of Cambridge, J J Thomson Avenue, Cambridge CB3 0HE, U.K.
- ⁵ Atacama Large Millimeter/submillimeter Array, ALMA Santiago Central Offices, Alonso de Cordova 3107, Vitacura, Casilla 763 0355, Santiago, Chile
- ⁶ CITA, University of Toronto, 60 St. George St., Toronto, ON M5S 3H8, Canada
- ⁷ CNRS, IRAP, 9 Av. colonel Roche, BP 44346, F-31028 Toulouse cedex 4, France
- ⁸ California Institute of Technology, Pasadena, California, U.S.A.
- ⁹ Centre of Mathematics for Applications, University of Oslo, Blindern, Oslo, Norway
- ¹⁰ DAMTP, University of Cambridge, Centre for Mathematical Sciences, Wilberforce Road, Cambridge CB3 0WA, U.K.
- ¹¹ DSM/Irfu/SPP, CEA-Saclay, F-91191 Gif-sur-Yvette Cedex, France
- ¹² DTU Space, National Space Institute, Juliane Mariesvej 30, Copenhagen, Denmark
- ¹³ Departamento de Física, Universidad de Oviedo, Avda. Calvo Sotelo s/n, Oviedo, Spain
- ¹⁴ Department of Astronomy and Astrophysics, University of Toronto, 50 Saint George Street, Toronto, Ontario, Canada
- ¹⁵ Department of Physics & Astronomy, University of British Columbia, 6224 Agricultural Road, Vancouver, British Columbia, Canada
- ¹⁶ Department of Physics, Gustaf Hällströmin katu 2a, University of Helsinki, Helsinki, Finland
- ¹⁷ Department of Physics, Princeton University, Princeton, New Jersey, U.S.A.
- ¹⁸ Department of Physics, Purdue University, 525 Northwestern Avenue, West Lafayette, Indiana, U.S.A.
- ¹⁹ Department of Physics, University of California, Berkeley, California, U.S.A.
- ²⁰ Department of Physics, University of California, One Shields Avenue, Davis, California, U.S.A.
- ²¹ Department of Physics, University of California, Santa Barbara, California, U.S.A.
- ²² Department of Physics, University of Illinois at Urbana-Champaign, 1110 West Green Street, Urbana, Illinois, U.S.A.
- ²³ Dipartimento di Fisica G. Galilei, Università degli Studi di Padova, via Marzolo 8, 35131 Padova, Italy
- ²⁴ Dipartimento di Fisica, Università La Sapienza, P. le A. Moro 2, Roma, Italy
- ²⁵ Dipartimento di Fisica, Università degli Studi di Milano, Via Celoria, 16, Milano, Italy
- ²⁶ Dipartimento di Fisica, Università degli Studi di Trieste, via A. Valerio 2, Trieste, Italy
- ²⁷ Dipartimento di Fisica, Università di Ferrara, Via Saragat 1, 44122 Ferrara, Italy
- ²⁸ Dipartimento di Fisica, Università di Roma Tor Vergata, Via della Ricerca Scientifica, 1, Roma, Italy
- ²⁹ Discovery Center, Niels Bohr Institute, Blegdamsvej 17, Copenhagen, Denmark
- ³⁰ Dpto. Astrofísica, Universidad de La Laguna (ULL), E-38206 La Laguna, Tenerife, Spain
- ³¹ European Southern Observatory, ESO Vitacura, Alonso de Cordova 3107, Vitacura, Casilla 19001, Santiago, Chile
- ³² European Space Agency, ESAC, Planck Science Office, Camino bajo del Castillo, s/n, Urbanización Villafranca del Castillo, Madrid, Spain

Villanueva de la Cañada, Madrid, Spain

Road, Manchester, M13 9PL, U.K.

- ³³ European Space Agency, ESTEC, Keplerlaan 1, 2201 AZ Noordwijk, The Netherlands
- ³⁴ Harvard-Smithsonian Center for Astrophysics, 60 Garden Street, Cambridge, MA 02138, U.S.A.
- ³⁵ Helsinki Institute of Physics, Gustaf Hållströmin katu 2, University of Helsinki, Helsinki, Finland
- ³⁶ INAF - Osservatorio Astrofisico di Catania, Via S. Sofia 78, Catania, Italy
- ³⁷ INAF - Osservatorio Astronomico di Padova, Vicolo dell'Osservatorio 5, Padova, Italy
- ³⁸ INAF - Osservatorio Astronomico di Roma, via di Frascati 33, Monte Porzio Catone, Italy
- ³⁹ INAF - Osservatorio Astronomico di Trieste, Via G.B. Tiepolo 11, Trieste, Italy
- ⁴⁰ INAF/IASF Bologna, Via Gobetti 101, Bologna, Italy
- ⁴¹ INAF/IASF Milano, Via E. Bassini 15, Milano, Italy
- ⁴² INRIA, Laboratoire de Recherche en Informatique, Université Paris-Sud 11, Bâtiment 490, 91405 Orsay Cedex, France
- ⁴³ IPAG: Institut de Planétologie et d'Astrophysique de Grenoble, Université Joseph Fourier Grenoble 1 / CNRS-INSU, UMR 5274, Grenoble, F-38041, France
- ⁴⁴ Imperial College London, Astrophysics group, Blackett Laboratory, Prince Consort Road, London, SW7 2AZ, U.K.
- ⁴⁵ Infrared Processing and Analysis Center, California Institute of Technology, Pasadena, CA 91125, U.S.A.
- ⁴⁶ Institut Néel, CNRS, Université Joseph Fourier Grenoble I, 25 rue des Martyrs, Grenoble, France
- ⁴⁷ Institut d'Astrophysique Spatiale, CNRS (UMR8617) Université Paris-Sud 11, Bâtiment 121, Orsay, France
- ⁴⁸ Institut d'Astrophysique de Paris, CNRS UMR7095, Université Pierre & Marie Curie, 98 bis boulevard Arago, Paris, France
- ⁴⁹ Institute of Astronomy and Astrophysics, Academia Sinica, Taipei, Taiwan
- ⁵⁰ Institute of Astronomy, University of Cambridge, Madingley Road, Cambridge CB3 0HA, U.K.
- ⁵¹ Institute of Theoretical Astrophysics, University of Oslo, Blindern, Oslo, Norway
- ⁵² Instituto de Astrofísica de Canarias, C/Vía Láctea s/n, La Laguna, Tenerife, Spain
- ⁵³ Instituto de Física de Cantabria (CSIC-Universidad de Cantabria), Avda. de los Castros s/n, Santander, Spain
- ⁵⁴ Jet Propulsion Laboratory, California Institute of Technology, 4800 Oak Grove Drive, Pasadena, California, U.S.A.
- ⁵⁵ Jodrell Bank Centre for Astrophysics, Alan Turing Building, School of Physics and Astronomy, The University of Manchester, Oxford
- ⁵⁶ Kavli Institute for Cosmology Cambridge, Madingley Road, Cambridge, CB3 0HA, U.K.
- ⁵⁷ LERMA, CNRS, Observatoire de Paris, 61 Avenue de l'Observatoire, Paris, France
- ⁵⁸ Laboratoire AIM, IRFU/Service d'Astrophysique - CEA/DSM - CNRS - Université Paris Diderot, Bât. 709, CEA-Saclay, F-91191 Gif-sur-Yvette Cedex, France
- ⁵⁹ Laboratoire Traitement et Communication de l'Information, CNRS (UMR 5141) and Télécom ParisTech, 46 rue Barrault F-75634 Paris Cedex 13, France
- ⁶⁰ Laboratoire de Physique Subatomique et de Cosmologie, CNRS/IN2P3, Université Joseph Fourier Grenoble I, Institut National Polytechnique de Grenoble, 53 rue des Martyrs, 38026

Grenoble cedex, France

- ⁶¹ Laboratoire de l'Accélérateur Linéaire, Université Paris-Sud 11, CNRS/IN2P3, Orsay, France
- ⁶² Lawrence Berkeley National Laboratory, Berkeley, California, U.S.A.
- ⁶³ Max-Planck-Institut für Astrophysik, Karl-Schwarzschild-Str. 1, 85741 Garching, Germany
- ⁶⁴ Max-Planck-Institut für Radioastronomie, Auf dem Hügel 69, 53121 Bonn, Germany
- ⁶⁵ MilliLab, VTT Technical Research Centre of Finland, Tietotie 3, Espoo, Finland
- ⁶⁶ National University of Ireland, Department of Experimental Physics, Maynooth, Co. Kildare, Ireland
- ⁶⁷ Niels Bohr Institute, Blegdamsvej 17, Copenhagen, Denmark
- ⁶⁸ Observational Cosmology, Mail Stop 367-17, California Institute of Technology, Pasadena, CA, 91125, U.S.A.
- ⁶⁹ Optical Science Laboratory, University College London, Gower Street, London, U.K.
- ⁷⁰ SISSA, Astrophysics Sector, via Bonomea 265, 34136, Trieste, Italy
- ⁷¹ SUPA, Institute for Astronomy, University of Edinburgh, Royal Observatory, Blackford Hill, Edinburgh EH9 3HJ, U.K.
- ⁷² School of Physics and Astronomy, Cardiff University, Queens Buildings, The Parade, Cardiff, CF24 3AA, U.K.
- ⁷³ Space Sciences Laboratory, University of California, Berkeley, California, U.S.A.
- ⁷⁴ Spitzer Science Center, 1200 E. California Blvd., Pasadena, California, U.S.A.
- ⁷⁵ Stanford University, Dept of Physics, Varian Physics Bldg, 382 Via Pueblo Mall, Stanford, California, U.S.A.
- ⁷⁶ Université de Toulouse, UPS-OMP, IRAP, F-31028 Toulouse cedex 4, France
- ⁷⁷ Universities Space Research Association, Stratospheric Observatory for Infrared Astronomy, MS 211-3, Moffett Field, CA 94035, U.S.A.
- ⁷⁸ University of Granada, Departamento de Física Teórica y del Cosmos, Facultad de Ciencias, Granada, Spain
- ⁷⁹ University of Miami, Knight Physics Building, 1320 Campo Sano Dr., Coral Gables, Florida, U.S.A.
- ⁸⁰ Warsaw University Observatory, Aleje Ujazdowskie 4, 00-478 Warszawa, Poland